

Banner appropriate to article type will appear here in typeset article

# 1 Turbulent cascade in fully developed 2 turbulent channel flow

3 **A. Apostolidis<sup>1</sup>, J. P. Laval<sup>1</sup> and J. C. Vassilicos<sup>1†</sup>**

4 <sup>1</sup>Univ. Lille, CNRS, ONERA, Arts et Metiers Institute of Technology, Centrale Lille, UMR  
5 9014 - LMFL - Laboratoire de Mécanique des Fluides de Lille - Kampé de Fériet, F-59000  
6 Lille, France

7 (Received xx; revised xx; accepted xx)

---

8 We show that Kolmogorov scale-by-scale equilibrium in the intermediate layer of  
9 fully developed turbulent channel flow is only achieved asymptotically around the  
10 Taylor length and, therefore, not in an inertial range. Furthermore, we analyse  
11 scale-by-scale turbulence production and interscale turbulence energy transfer in  
12 terms of alignments/anti-alignments of fluctuating velocities, straining/compressive  
13 relative motions, forward/inverse interscale transfer/cascade and homogeneous/non-  
14 homogeneous interscale transfer rate contributions. We also propose leading order  
15 scalings for second and third order two-point statistics, including the extremum  
16 interscale turbulence energy transfer rate and a second order anisotropic structure  
17 function, which acts as a scale-by-scale Reynolds shear stress and determines the  
18 scale-by-scale (two-point) turbulence production rate.

19 **Key words:**

---

## 20 **1. Introduction**

21 The Kolmogorov theory of equilibrium cascade works best for statistically stationary  
22 and homogeneous turbulence where the power input balances the dissipation rate and  
23 predicts that the interscale transfer rate balances the turbulence dissipation rate in  
24 an inertial range of scales (Batchelor 1953; Frisch 1995; Lesieur 1997). In particular,  
25 this inertial range equilibrium cascade leads to the well-known turbulence dissipation  
26 scaling (Batchelor 1953; Sreenivasan 1984; Vassilicos 2015) first introduced by Tay-  
27 lor (1935) without justification. In statistically homogeneous but non-stationary, in  
28 particular decaying, turbulence, the situation is different. Specifically, there is a non-  
29 equilibrium turbulence dissipation scaling initially during decay, (Vassilicos 2015; Goto  
30 & Vassilicos 2016) followed at later times by the classical turbulence dissipation as a  
31 result of balanced non-equilibrium (Goto & Vassilicos 2016; Steiros 2022) rather than  
32 Kolmogorov equilibrium throughout an inertial range.

† Email address for correspondence: john-christos.vassilicos@centralelille.fr

33 Lundgren (2002) applied a matched asymptotic expansion approach to freely decaying  
 34 homogeneous isotropic turbulence far from initial conditions, which led to the conclu-  
 35 sion that the interscale transfer rate has an extremum at a length scale  $r_{max}$  that is  
 36 proportional to the Taylor length  $\lambda$ . Wind tunnel data of nominally freely decaying  
 37 homogeneous isotropic turbulence (Obligado & Vassilicos 2019) confirm  $r_{max} \approx 1.5\lambda$  and  
 38 EDQNM simulations of such turbulence (Meldi & Vassilicos 2021) confirm  $r_{max} \approx 1.12\lambda$   
 39 for  $Re_\lambda = 10^2$  to  $10^6$ . Hence, Kolmogorov equilibrium in non-stationary, in fact freely  
 40 decaying far from initial conditions, statistically homogeneous isotropic turbulence seems  
 41 to be achieved asymptotically only around  $\lambda$ ; and not in an inertial range given that  $\lambda$   
 42 depends on viscosity and total turbulent kinetic energy and that there is a systematic  
 43 departure from equilibrium (most clearly demonstrated in Meldi & Vassilicos (2021))  
 44 when moving away from  $\lambda$ , both towards the integral scale and towards the Kolmogorov  
 45 length  $\eta$ .

46 Diverting attention from homogeneous non-stationary turbulence to stationary non-  
 47 homogeneous turbulence, we ask about the validity of Kolmogorov equilibrium in sta-  
 48 tionary non-homogeneous conditions and chose to focus in this paper on fully developed  
 49 turbulent channel flow (FD TCF). This is a statistically stationary non-homogeneous tur-  
 50 bulent flow where turbulence production approximately balances turbulence dissipation  
 51 (similarly to statistically stationary homogeneous turbulence) in some very significant  
 52 region of space, the intermediate layer where the log-law of the wall has been traditionally  
 53 claimed. Is there an average equilibrium between interscale turbulence energy transfer  
 54 rate and turbulence dissipation in the intermediate layer of FD TCF where turbulence  
 55 production approximately balances turbulence dissipation? If so, in what range of length  
 56 scales, inertial or not? What processes are involved in the scale-by-scale turbulence  
 57 energy balance in that range, if there is one, and outside it? What is the role of  
 58 inhomogeneity, in particular in terms of scale-by-scale turbulence production but also  
 59 directly on interscale energy transfer? What type of flow motions underpin interscale  
 60 turbulence energy transfers and scale-by-scale turbulence production (referred to as two-  
 61 point turbulence production in the remainder of this paper)?

62 In the following section, we introduce the scale-by-scale turbulence energy balance  
 63 in its most general form and the spherical average operation, which we use to simplify  
 64 it for this study. Section 3 is a brief description of the FD TCF DNS data we utilize  
 65 for our post-processing. In section 4 we simplify the spherically averaged scale-by-scale  
 66 turbulence energy balance for the particular case of the intermediate layer of a FD TCF  
 67 and in section 5 we examine the two-point turbulence production term which appears  
 68 in this balance. Section 6 deals with second and third order structure functions and  
 69 interscale turbulence energy transfer by adapting to FD TCF the matched asymptotic  
 70 expansion approach of Lundgren (2002), and then we compare the results to the DNS data  
 71 in section 7. Finally, section 8 introduces two decompositions of the interscale turbulence  
 72 energy transfer rate and attempts to answer the questions of non-homogeneity's role and  
 73 of what flow motions are responsible for which aspects of interscale turbulence energy  
 74 transfer. In the paper's last section, we summarise our conclusions.

## 75 2. Scale-by-scale turbulence energy balance

76 To analyse the turbulent energy cascade in turbulent channel flow, we utilize a  
 77 Kármán–Howarth–Monin–Hill (KHMH) equation which is a scale-by-scale energy budget  
 78 equation in its most general form without any assumptions about the flow (Hill 2001,  
 79 2002). The form of KHMH equation that we use is an evolution equation for  $|\delta\mathbf{u}|^2$ ,  
 80 where  $\delta\mathbf{u} \equiv \mathbf{u}(\mathbf{x} + \mathbf{r}/2, t) - \mathbf{u}(\mathbf{x} - \mathbf{r}/2, t)$  is the difference between fluctuating velocities

81 at two points  $\boldsymbol{\xi}^+ \equiv \boldsymbol{x} + \boldsymbol{r}/2$  and  $\boldsymbol{\xi}^- \equiv \boldsymbol{x} - \boldsymbol{r}/2$  in the flow where the separation vector  
 82  $\boldsymbol{r} = (r_1, r_2, r_3)$  gives some sense of scales. The centroid  $\boldsymbol{x} = (x_1, x_2, x_3)$  is mid-way  
 83 between these two points.

A Reynolds decomposition  $\boldsymbol{U} + \boldsymbol{u}$  is used for the velocity field in this form of the KHMH equation where  $\boldsymbol{U} = (U_1, U_2, U_3)$  is the mean flow. The KHMH equation follows directly from the incompressible Navier-Stokes equations and, with notations  $U_i^\pm \equiv U_i(\boldsymbol{x} \pm \boldsymbol{r}/2)$ ,  $u_i^\pm \equiv u_i(\boldsymbol{x} \pm \boldsymbol{r}/2)$  and  $\delta p \equiv p(\boldsymbol{x} + \boldsymbol{r}/2, t) - p(\boldsymbol{x} - \boldsymbol{r}/2, t)$  where  $p$  is the fluctuating pressure field, reads as follows:

$$\begin{aligned}
 & \underbrace{\frac{\partial \langle |\delta \boldsymbol{u}|^2 \rangle}{\partial t}}_{A_t} + \underbrace{\frac{U_i^+ + U_i^-}{2} \frac{\partial \langle |\delta \boldsymbol{u}|^2 \rangle}{\partial x_i}}_A + \underbrace{\frac{\partial \langle \delta u_i |\delta \boldsymbol{u}|^2 \rangle}{\partial r_i}}_II + \underbrace{\frac{\partial \delta U_i \langle |\delta \boldsymbol{u}|^2 \rangle}{\partial r_i}}_{II_U} = \\
 & \underbrace{-2 \langle \delta u_i \delta u_j \rangle \frac{\partial \delta U_j}{\partial r_i} - \langle (u_i^+ + u_i^-) \delta u_j \rangle \frac{\partial \delta U_j}{\partial x_i}}_P - \underbrace{\frac{\partial \langle \frac{u_i^+ + u_i^-}{2} |\delta \boldsymbol{u}|^2 \rangle}{\partial x_i}}_{T_u} - \underbrace{2 \frac{\partial \langle \delta u_i \delta p \rangle}{\partial x_i}}_{T_p} \\
 & + \underbrace{\nu \frac{1}{2} \frac{\partial^2 \langle |\delta \boldsymbol{u}|^2 \rangle}{\partial x_i^2}}_{D_x} + \underbrace{2\nu \frac{\partial^2 \langle |\delta \boldsymbol{u}|^2 \rangle}{\partial r_i^2}}_{D_r} - \underbrace{\left[ 2\nu \langle (\partial u_j^- / \partial \xi_i^-)^2 \rangle + 2\nu \langle (\partial u_j^+ / \partial \xi_i^+)^2 \rangle \right]}_\varepsilon
 \end{aligned} \tag{2.1}$$

85 where the brackets  $\langle \cdot \rangle$  denote the averaging operation on which the Reynolds decompo-  
 86 sition is based. The KHMH equation includes the following terms:

- 87 •  $A_t = \frac{\partial \langle |\delta \boldsymbol{u}|^2 \rangle}{\partial t}$  is the time derivative term.
- 88 •  $A = \frac{U_i^+ + U_i^-}{2} \frac{\partial \langle |\delta \boldsymbol{u}|^2 \rangle}{\partial x_i}$  is the mean advection term.
- 89 •  $II = \frac{\partial \langle \delta u_i |\delta \boldsymbol{u}|^2 \rangle}{\partial r_i}$  is the nonlinear interscale transfer rate of  $|\delta \boldsymbol{u}|^2$  by turbulent  
 90 fluctuations in scale space and thus directly linked to the energy cascade.
- 91 •  $II_U = \frac{\partial \delta U_i \langle |\delta \boldsymbol{u}|^2 \rangle}{\partial r_i}$  is the linear interscale transfer rate of  $|\delta \boldsymbol{u}|^2$  in scale space by mean  
 92 velocity differences.
- 93 •  $P = -2 \langle \delta u_i \delta u_j \rangle \frac{\partial \delta U_j}{\partial r_i} - \langle (u_i^+ + u_i^-) \delta u_j \rangle \frac{\partial \delta U_j}{\partial x_i}$  is the two-point production of  $|\delta \boldsymbol{u}|^2$  by  
 94 the mean shear.
- 95 •  $T_u = \frac{\partial \langle \frac{u_i^+ + u_i^-}{2} |\delta \boldsymbol{u}|^2 \rangle}{\partial x_i}$  is the turbulent transport of  $|\delta \boldsymbol{u}|^2$  in physical space.
- 96 •  $T_p = 2 \frac{\partial \langle \delta u_i \delta p \rangle}{\partial x_i}$  is the pressure-velocity term.
- 97 •  $D_x = \frac{\nu}{2} \frac{\partial^2 \langle |\delta \boldsymbol{u}|^2 \rangle}{\partial x_i^2}$  is the viscous diffusion in physical space.
- 98 •  $D_r = 2\nu \frac{\partial^2 \langle |\delta \boldsymbol{u}|^2 \rangle}{\partial r_i^2}$  is the viscous diffusion in scale space.
- 99 •  $\varepsilon = 2\nu \langle (\partial u_j^- / \partial \xi_i^-)^2 \rangle + 2\nu \langle (\partial u_j^+ / \partial \xi_i^+)^2 \rangle$  is the two-point averaged turbulence  
 100 pseudo-dissipation rate which is very close to the actual turbulence dissipation rate (e.g.  
 101 see Pope 2000).

102 At this stage we specialise this equation to FD TCF by choosing the averaging operation  
 103  $\langle \cdot \rangle$  to be over the streamwise and spanwise homogeneous directions, i.e. over coordinates  
 104  $x \equiv x_1$  (streamwise) and  $z \equiv x_3$  (spanwise), and over time. The wall normal coordinate is  
 105  $y \equiv x_2$ . Note that  $U_2 = U_3 = 0$  and that this averaging operation implies  $A_t = 0 = A$ . In  
 106 non-homogeneous and non-isotropic turbulent flows (such as FD TCF) energy transfers  
 107 and exchanges, including the turbulence cascade, are anisotropic. This equation has been  
 108 studied extensively in FD TCF by Marati *et al.* (2004); Cimarelli & De Angelis (2012);  
 109 Cimarelli *et al.* (2013, 2016); Gatti *et al.* (2019). In this paper we concentrate our interest  
 110 on the directionally-averaged energy transfers by applying to each term of the KHMH

---

Name	$Re_\tau$	$L_x/\delta$	$L_z/\delta$	$\Delta x^+$	$\Delta z^+$	$N_y$	$dt^+$	$N_t$
LJ950	932	$2\pi$	$\pi$	11.5	5.7	385	8	3151
LJ2000	2003	$2\pi$	$\pi$	12.3	6.2	633	25	462

---

TABLE 1. DNS databases

111 equation an additional average over spheres in  $\mathbf{r}$ -space. We therefore work with

$$112 \quad \Pi^v + \Pi_U^v = \mathcal{P}^v + T_u^v + T_p^v + D_x^v + D_r^v - \varepsilon^v \quad (2.2)$$

113 where (following Zhou & Vassilicos (2020) and section 2 of Chen & Vassilicos (2022))  
 114 every term is obtained from its analogue in equation 2.1 by the application of the  
 115 normalised 3D integral  $\frac{3}{4\pi r^3} \int_{S(r)} d^3\mathbf{r}$ ,  $S(r)$  being the sphere of radius  $r$  in  $\mathbf{r}$ -space; for  
 116 example  $\Pi^v \equiv \frac{3}{4\pi r^3} \int_{S(r)} \Pi d^3\mathbf{r}$ ,  $\Pi_U^v \equiv \frac{3}{4\pi r^3} \int_{S(r)} \Pi_U d^3\mathbf{r}$ ,  $\mathcal{P}^v \equiv \frac{3}{4\pi r^3} \int_{S(r)} \mathcal{P} d^3\mathbf{r}$ , etc.

117 This approach averages over and therefore ignores length-scale anisotropies and re-  
 118 places  $\mathbf{r}$  by its modulus  $r = |\mathbf{r}|$  as a single measure of length-scale. However, the  
 119 fundamental anisotropy responsible for correlations between streamwise and wall-normal  
 120 directions remains in the turbulence production term. Every term in equation 2.2 is a  
 121 function of only  $y$  (spatial non-homogeneity variable) and  $r$  (length-scale variable).

122 In the following section we describe the data from Direct Numerical Simulations (DNS)  
 123 of FD TCF that we use in this paper. We describe this DNS data before starting our  
 124 analysis of equation 2.2 in order to be able to test against this data certain aspects of  
 125 our analysis as it proceeds.

### 126 3. DNS data

127 For our analysis we utilize the DNS data of Lozano-Durán & Jiménez (2014) for FD  
 128 TCF at  $Re_\tau = 932$  and 2003, ( $Re_\tau \equiv u_\tau \delta / \nu$  where  $\nu$  is the kinematic viscosity,  $\delta$  is the  
 129 channel half-width, and  $u_\tau$  is the skin friction velocity obtained by averaging over time  
 130 and over streamwise coordinate  $x$  and spanwise coordinate  $z$  at the channel's solid wall  
 131  $y = 0$ ). The domain size for both simulations is  $L_x = 2\pi\delta$  in the streamwise and  $L_z = \pi\delta$   
 132 in the spanwise directions. The Navier-Stokes equations have been solved by integrating  
 133 the evolution equations in terms of the wall-normal vorticity and the Laplacian of the  
 134 wall-normal velocity for an incompressible fluid. The Fourier spectral method was used  
 135 for the spatial discretization in the wall parallel directions. For the discretisation in the  
 136 wall-normal direction, Chebyshev polynomials were used in the  $Re_\tau = 932$  case whereas  
 137 a seven-point compact finite difference scheme was used in the  $Re_\tau = 2003$  case. Finally,  
 138 a third-order semi-implicit Runge-Kutta method with CFL = 0.5 was chosen for time  
 139 advancement. A comparison of the two datasets can be found in Table 1 (the superscript  
 140  $^+$  refers to non-dimensionalisation with wall units  $\delta_\nu \equiv \nu/u_\tau$  for length and  $\delta_\nu/u_\tau$  for  
 141 time). We focus our DNS data analysis on the wall-normal locations that correspond to  
 142 the region where the average production rate of turbulent kinetic energy roughly balances  
 143 the average turbulence dissipation rate as identified by Apostolidis *et al.* (2022), i.e.  
 144  $60 \leq y^+ \leq Re_\tau/2$ .

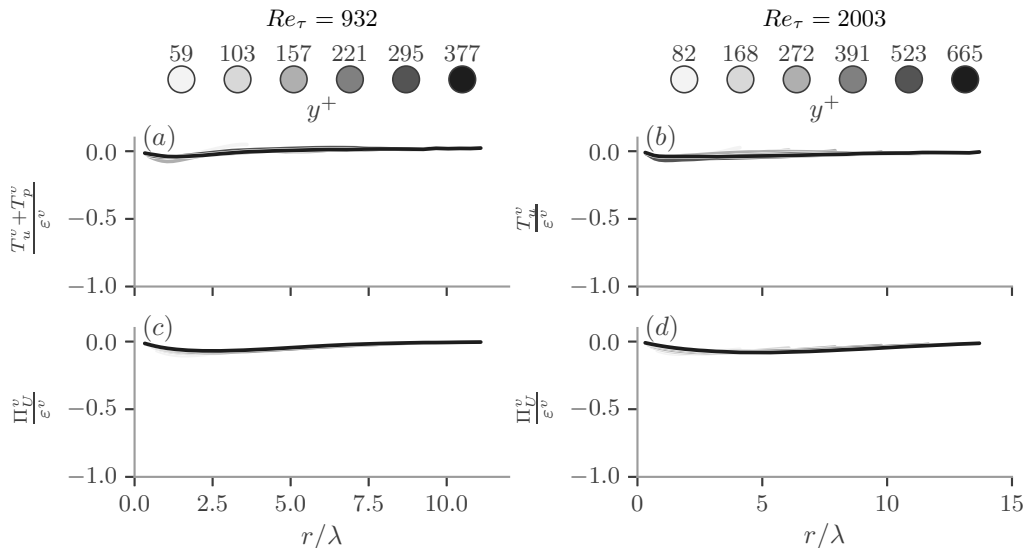


FIGURE 1. (a) Turbulent transport  $T_u$  plus pressure-velocity term  $T_p$ , integrated over the volume of sphere with radius  $r$ , normalised by the volume integral of the two point dissipation rate  $\varepsilon$  as a function of  $r/\lambda$  for  $Re_\tau = 932$ , (b)  $T_u^v/\varepsilon^v$  for  $Re_\tau = 2003$  ( $T_p$  is unavailable from the recorded DNS data at  $Re_\tau = 2003$ ), (c) volume integral of linear interscale transfer term divided with  $\varepsilon^v$   $\Pi_U^v/\varepsilon^v$  for  $Re_\tau = 932$ , (d) for  $Re_\tau = 2003$ . Wall-normal distance is increased from light to dark colors ( $y^+ = 59$  to  $377$  for  $Re_\tau = 932$ ,  $y^+ = 82$  to  $665$  for  $Re_\tau = 2003$ ). The normalisation by the Taylor length  $\lambda$  (defined in subsection 6.3) is arbitrary in these plots.

#### 145 4. Scale-by-scale turbulent energy balance in the one-point average 146 equilibrium range of FD TCF

147 We now examine equation 2.2 in the region of FD TCF, where the average one-point  
148 turbulence production rate is in approximate equilibrium with the average turbulence  
149 dissipation rate at a given  $y$ . This is a region of distances  $y$  from the bottom wall (where  
150  $y = 0$ ) such that  $\delta_\nu \ll y \ll \delta$  (in the limit  $Re_\tau = \delta/\delta_\nu \gg 1$ ) and where, classically,  
151 the mean flow velocity  $\mathbf{U} = (U_1, 0, 0)$  is expected to be logarithmic (e.g. see Pope  
152 2000). Whilst previous works have suggested some not insignificant deviations from a  
153 log dependence on  $y$  of  $U_1$  (e.g. see Vassilicos *et al.* 2015), in this work we assume that  
154 the log law accounts for most of  $U_1$  which implies that  $\Pi_U = \frac{\partial}{\partial r_1}(\delta U_1 \langle |\delta \mathbf{u}|^2 \rangle)$  is close to 0  
155 in the region  $\delta_\nu \ll y \ll \delta$  if  $r_2 \ll 2y$  because  $\delta U_1 = \frac{u_\tau}{\kappa} \ln \frac{1+r_2/y}{1-r_2/y} \approx 0$  ( $\kappa$  is the von Kármán  
156 dimensionless coefficient and note that wall blocking implies that  $r_2$  is necessarily smaller  
157 or equal to  $2y$ .) The DNS data confirm the prediction that  $\Pi_U^v$  is close to zero, see figure  
158 1(c,d). We also make the assumption that turbulence is well mixed in this region and  
159 therefore assume that the physical-space divergence term  $T_u^v + T_p^v$  is negligible. Whilst  
160 the DNS data support this assumption, see figure 1(a,b), it must be stressed that pressure  
161 plays an important redistributive role and that spatial energy transfer is not fully absent  
162 in the intermediate layer (e.g. Lozano-Durán & Jiménez 2014; Cimarelli *et al.* 2016;  
163 Lee & Moser 2019). The numerical details behind our calculations of normalised 3D  
164 integrals  $\frac{3}{4\pi r^3} \int_{S(r)} d^3 \mathbf{r}$ , and in particular of terms such as  $T_u^v = \frac{3}{4\pi r^3} \int_{S(r)} T_u d^3 \mathbf{r}$  and  
165  $T_p^v = \frac{3}{4\pi r^3} \int_{S(r)} T_p d^3 \mathbf{r}$ , are given in the Appendix.

166 We therefore neglect both  $\Pi_U^v$  and  $T_u^v + T_p^v$  from equation 2.2 and are left with

$$167 \quad \Pi^v \approx \mathcal{P}^v + D_x^v + D_r^v - \varepsilon^v \quad (4.1)$$

168 for  $r_2 \ll 2y$  in the intermediate layer  $\delta_\nu \ll y \ll \delta$ .

169 By application of the Gauss divergence theorem, the interscale transfer rate takes the  
170 form

$$171 \quad \Pi^v = \frac{3}{4\pi} \int \left\langle \frac{\delta \mathbf{u} \cdot \hat{\mathbf{r}}}{r} |\delta \mathbf{u}|^2 \right\rangle d\Omega_r \equiv \frac{S_3(r, y)}{r} \quad (4.2)$$

172 where  $\Omega_r$  is the solid angle in  $\mathbf{r}$  space and  $\hat{\mathbf{r}} \equiv \mathbf{r}/|\mathbf{r}|$ . By distinguishing between radial  
173 and solid angle integrations in  $\mathbf{r}$ -space, the viscous diffusion terms become

$$174 \quad D_x^v + D_r^v = \frac{3\nu}{8\pi r^3} \int_0^r \rho^2 \frac{d^2 S_2}{dy^2}(\rho, y) d\rho + \frac{3\nu}{\pi r} \frac{dS_2}{dr}(r, y) \quad (4.3)$$

175 where

$$176 \quad S_2(r, y) \equiv \int \langle |\delta \mathbf{u}|^2 \rangle d\Omega_r. \quad (4.4)$$

177 In FD TCF the production term  $\mathcal{P}^v$  is obtained by applying the integral operation  
178  $\frac{3}{4\pi r^3} \int_{S(r)} d^3 \mathbf{r}$  on  $-2 \langle \delta u_2 \delta u_1 \rangle \frac{\partial \delta U_1}{\partial r_2} - \langle (u_2^+ + u_1^-) \delta u_1 \rangle \frac{\partial \delta U_1}{\partial y}$ . Targeting again the intermediate  
179 region  $\delta_\nu \ll y \ll \delta$  where the log law  $\frac{dU_1}{dy} \approx \frac{u_\tau}{\kappa y}$  might be considered to be a good  
180 approximation in the limit  $\delta/\delta_\nu \gg 1$  ( $\kappa$  is the von Kármán dimensionless coefficient), the  
181 two-point production term becomes

$$182 \quad \mathcal{P}^v \approx -\frac{u_\tau^3}{\kappa y} \frac{3}{4\pi r^3} \int_0^r \rho^2 \left[ \frac{S_{12}(\rho, y)}{u_\tau^2} - \frac{S_{1 \times 2}(\rho, y)}{u_\tau^2} \right] d\rho \quad (4.5)$$

183 in this intermediate region, where

$$184 \quad S_{12}(r, y) \equiv 2 \int \langle \delta u_2 \delta u_1 \rangle \left[ 1 - \left( \frac{r_2}{2y} \right)^2 \right]^{-1} d\Omega_r \quad (4.6)$$

185 and

$$186 \quad S_{1 \times 2}(r, y) \equiv \int \langle (u_2^+ + u_2^-) \delta u_1 \rangle (r_2/y) \left[ 1 - \left( \frac{r_2}{2y} \right)^2 \right]^{-1} d\Omega_r. \quad (4.7)$$

187 We expect  $S_{1 \times 2}(r, y)$  to be much smaller in magnitude than  $S_{12}(r, y)$ , in fact even  
188 close to vanishing, because of the expected decorrelation between wall-normal velocity  
189 fluctuations effectively larger than  $r$  (i.e.  $u_2^+ + u_2^-$ ) and streamwise velocity fluctuations  
190 effectively smaller than  $r$  (i.e.  $\delta u_1$ ). This is confirmed by the DNS data in figure 2,  
191 which also show that  $S_{12}(r, y)$  is negative for all  $r \leq 2y$  irrespective of  $y$  (because of  
192 wall blocking,  $r$  cannot be larger than  $2y$ , and because of the integrand's singularity in  
193 the definitions of  $S_{1 \times 2}(r, y)$  and  $S_{12}(r, y)$  we plot them for  $r \leq 2y - 8\delta_\nu$  throughout the  
194 paper). In the intermediate region where the log law of the wall might be expected to hold  
195 we therefore have a positive two-point production term given, to good approximation,  
196 by

$$197 \quad \mathcal{P}^v \approx -\frac{u_\tau^3}{\kappa y} \frac{3}{4\pi r^3} \int_0^r \rho^2 \frac{S_{12}(\rho, y)}{u_\tau^2} d\rho. \quad (4.8)$$

198 Bringing together 4.2, 4.3 and 4.8 into equation 4.1 we obtain the following two-point  
199 energy balance valid for  $r_2 \ll 2y$  and  $\delta/\delta_\nu \gg 1$  in the intermediate region  $\delta_\nu \ll y \ll \delta$  of  
200 FD TCF:

$$\frac{S_3(r, y)}{r} - \frac{3\nu}{8\pi r^3} \int_0^r \rho^2 \frac{d^2 S_2}{dy^2}(\rho, y) d\rho + \frac{3\nu}{\pi r} \frac{dS_2}{dr}(r, y) \approx -\varepsilon^v - \frac{u_\tau^3}{\kappa y} \frac{3}{4\pi r^3} \int_0^r \rho^2 S_{12}(\rho, y) d\rho. \quad (4.9)$$

201 In this equation, the first term on the left-hand side is the interscale transfer rate,  
202

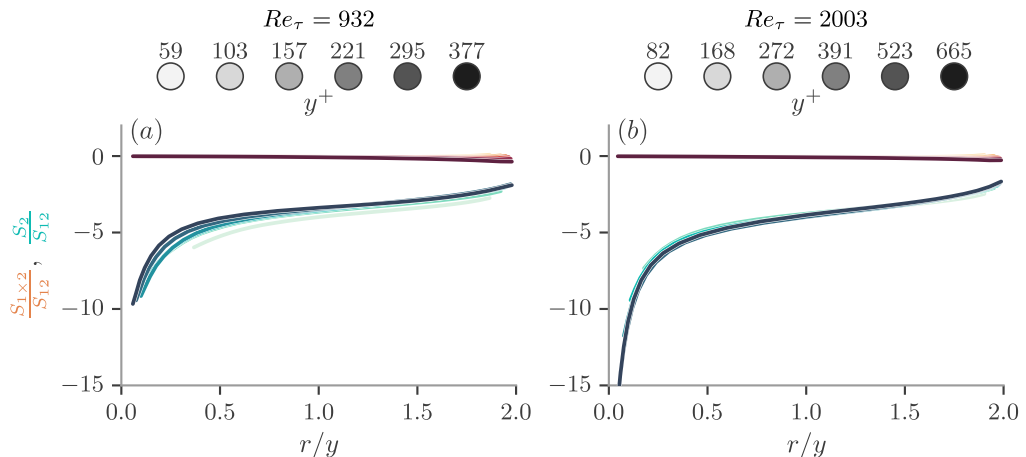


FIGURE 2. Ratios of  $S_{1 \times 2}$  in orange colors and  $S_2$  in marine colors over  $S_{12}$  for different normalised scales  $r/y$ . Wall-normal distance is increased from light to dark colors as in figure 1. (a)  $Re_\tau = 932$ , (b)  $Re_\tau = 2003$ .

203 the second and third terms on the left-hand side are the viscous diffusion terms and the  
 204 second term on the right-hand side is the two-point turbulence production rate. Before  
 205 making use of this equation in the section after next, we look closer into the positive sign  
 206 of the two-point turbulence production.

## 207 5. Two-point turbulence production

208  $\mathcal{P}^v$  represents the rate with which turbulent kinetic energy is gained or lost by scales  
 209 smaller than  $r$  if  $\mathcal{P}^v$  is respectively positive or negative. Of course, we may expect energy  
 210 to be gained in some  $\mathbf{r}$  directions and lost in some other  $\mathbf{r}$  directions:  $\mathcal{P}^v$  represents the  
 211 rate with which the aggregate energy averaged over all directions is gained or lost at  
 212 scales smaller than  $r$  by the linear effects of mean flow gradients on the turbulence. This  
 213 is not a non-linear interscale mechanism relating to a turbulence cascade which is, in  
 214 fact, represented by  $H^v$ .

215 Turbulence production results from the interplay of non-isotropy in the form of non-  
 216 zero Reynolds shear stresses with the mean flow gradient. In FD TCF the one-point  
 217 Reynolds shear stress is  $\langle u_1 u_2 \rangle$  and it interacts with the mean flow gradient  $\frac{dU_1}{dx_2} = \frac{dU_1}{dy}$   
 218 to give the one-point turbulence production rate  $-\langle u_1 u_2 \rangle \frac{dU_1}{dy}$  which is positive (i.e.  
 219 creation of turbulent kinetic energy) because  $\langle u_1 u_2 \rangle$  is negative. The negative sign  
 220 of  $\langle u_1 u_2 \rangle$  results from the predominance of turbulent transport towards the wall of  
 221 forward streamwise fluctuating velocities and of turbulent transport away from the wall of  
 222 backward streamwise fluctuating velocities. These turbulent momentum fluxes are partly  
 223 caused by sweeps in the case of transport towards the wall and ejections in the case of  
 224 transport away from the wall (Wallace 2016; Kline & Robinson 1990) and lead to the  
 225 well-known increase by turbulence of wall shear stress and skin friction drag.

226 The two-point Reynolds shear stress  $\langle \delta u_1 \delta u_2 \rangle$  results from anisotropies at scales  
 227 comparable to  $r$  and smaller and relates to the one-point shear stress by

$$228 \quad \langle \delta u_1 \delta u_2 \rangle = (\langle u_1^+ u_2^+ \rangle - \langle u_1^+ u_2^- \rangle) + (\langle u_1^- u_2^- \rangle - \langle u_1^- u_2^+ \rangle). \quad (5.1)$$

229 One can expect the two-point Reynolds shear stress to have the same sign as the one-  
 230 point shear stresses at  $\xi^+$  and  $\xi^-$  (which are known to be negative in FD TCF) if the

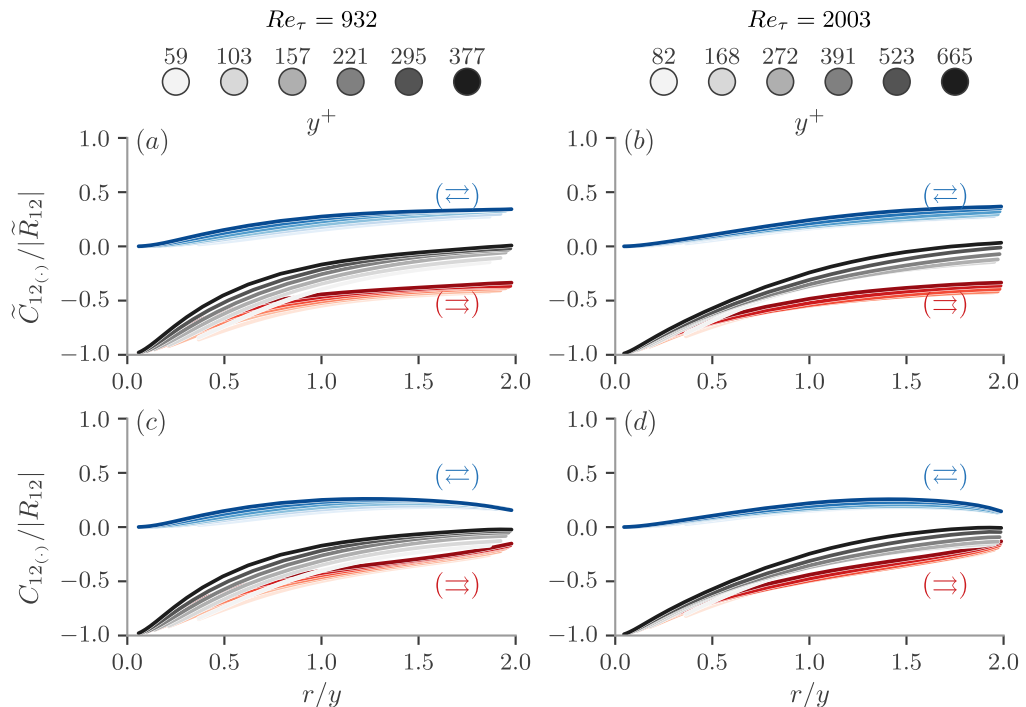


FIGURE 3. (a, b)  $\tilde{C}_{12}/|\tilde{R}_{12}|$  integrated over the whole sphere in black lines, conditionally integrated over anti-aligned pairs in blue lines, and conditionally integrated over aligned pairs in red lines. (a)  $Re_\tau = 932$ , (b)  $Re_\tau = 2003$ . (c, d) Similarly for  $C_{12}/|R_{12}|$ . Wall-normal distance is increased from light to dark colors as in figure 1.

231 magnitudes of the two-point correlations  $\langle u_1^+ u_2^- \rangle$  and  $\langle u_1^- u_2^+ \rangle$  are decreasing functions of  
 232 distance between  $\xi^+$  and  $\xi^-$ . The two-point Reynolds shear stress appears in the two-  
 233 point turbulence production rate via  $S_{12}$  (see equation 4.8 and the definition 4.6 of  $S_{12}$ )  
 234 and we therefore define, for initial simplicity of interpretation, a two-point Reynolds shear  
 235 stress integrated over the solid angle in  $\mathbf{r}$ -space as follows:  $\tilde{S}_{12}(r, y) \equiv \int \langle \delta u_2 \delta u_1 \rangle d\Omega_r$ .  
 236 Defining additionally  $\int \langle u_2^+ u_1^+ \rangle d\Omega_r = \int \langle u_2^- u_1^- \rangle d\Omega_r \equiv \tilde{R}_{12}(y, r)$  and  $\int \langle u_2^+ u_1^- \rangle d\Omega_r =$   
 237  $\int \langle u_2^- u_1^+ \rangle d\Omega_r \equiv \tilde{C}_{12}(r, y)$ , relation 5.1 leads to

$$238 \quad \tilde{S}_{12}(r, y) = 2\tilde{R}_{12}(y, r) - 2\tilde{C}_{12}(r, y) \quad (5.2)$$

239 in terms of solid angle-integrated one-point Reynolds shear stress  $\tilde{R}_{12}(y, r)$  and solid  
 240 angle-integrated two-point correlation  $\tilde{C}_{12}(r, y)$ . In figure 3(a,b) we use the DNS data to  
 241 plot  $\tilde{C}_{12}(r, y)/|\tilde{R}_{12}(y, r)|$  versus  $r$  (black lines) for the two Reynolds numbers available and  
 242 for different values of wall distance  $y$ . In all cases  $\tilde{C}_{12}(r, y)/|\tilde{R}_{12}(y, r)|$  is a monotonically  
 243 increasing function of  $r$ , from  $\tilde{C}_{12}(r, y)/|\tilde{R}_{12}(y, r)| = -1$  at  $r = 0$  towards 0 with  
 244 increasing  $r$ . It follows from 5.2 that the solid angle-integrated two-point Reynolds stress  
 245 inherits the negative sign of the solid angle-integrated one-point Reynolds shear stress  
 246 but with reduced magnitude because of the negative two-point correlation  $\tilde{C}_{12}(r, y)$  which  
 247 is smaller in magnitude than  $\tilde{R}_{12}(y, r)$  for all  $y$  and all  $r \neq 0$ .

248 Inheriting the sign of the one-point Reynolds shear stress means for the two-point  
 249 Reynolds shear stress that sweeps and ejections are contributing to its negative sign.  
 250 However the two-point correlation  $\tilde{C}_{12}(r, y)$  reduces the proportion of this contribution.



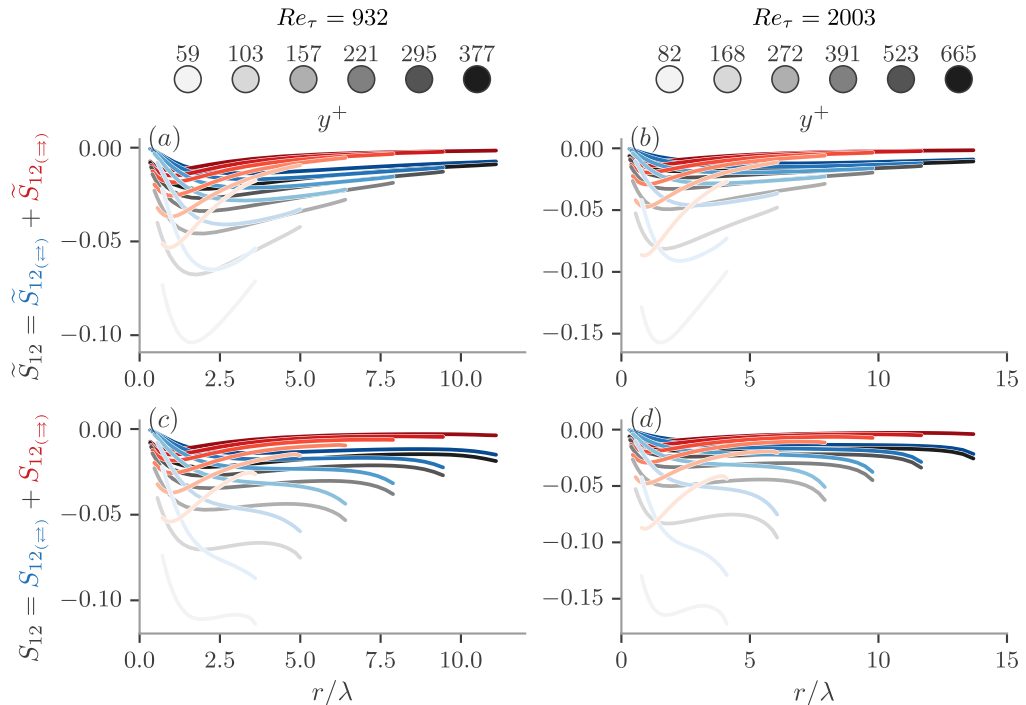


FIGURE 4. (a, b)  $\tilde{S}_{12}$  integrated over the whole sphere in black lines, conditionally integrated over anti-aligned pairs in blue lines, and conditionally integrated over aligned pairs in red lines. (a)  $Re_\tau = 932$ , (b)  $Re_\tau = 2003$ . (c, d) Similarly for  $S_{12}$ . Wall-normal distance is increased from light to dark colors as in figure 1. The Taylor length  $\lambda$  is defined in subsection 6.3.

251 Assuming that fluctuating velocities may be approximately aligned within sweep and  
 252 ejection events, particularly for the smaller values of  $r$ , we now use the DNS data to  
 253 calculate correlations between  $u_2$  and  $u_1$  at two different points  $\xi^+$  and  $\xi^-$  conditionally  
 254 on  $\mathbf{u}^+ \cdot \mathbf{u}^- > 0$  for aligned pairs of fluctuating velocities and conditionally on  $\mathbf{u}^+ \cdot$   
 255  $\mathbf{u}^- < 0$  for anti-aligned pairs. We compute the resulting solid angle-integrated conditional  
 256 correlations which we plot in figure 3(a,b) normalised by  $|\tilde{R}_{12}(y, r)|$  and identify them by  
 257  $(\Rightarrow)$  for the aligned and  $(\Leftarrow)$  for the anti-aligned condition. For both Reynolds numbers  
 258 and for all wall distances tested, the conditional correlations are increasing functions of  
 259  $r$  but positive when the condition is anti-alignment and negative when the condition  
 260 is alignment. Anti-alignment, which is not so expected within sweeps and ejections (but  
 261 may be linked to sweep-ejection pairs), increases the magnitude of the negative value of  
 262  $\tilde{S}_{12}(r, y)$ , particularly at the larger separations  $r$ , whereas alignment, presumably more  
 263 present within sweeps and ejections, actually contributes to reduce the magnitude of  
 264 the negative value of  $\tilde{S}_{12}(r, y)$ . As a result, the part of  $-\tilde{S}_{12}(r, y)$  that is conditional on  
 265 aligned fluctuating velocities is smaller than the part of  $-\tilde{S}_{12}(r, y)$  which is conditional  
 266 on anti-aligned fluctuating velocities, particularly at values of  $r$  larger than the Taylor  
 267 length-scale (see figure 4). The actual role of the Taylor length appears in the following  
 268 section.

269 The two-point Reynolds shear stress determines two-point turbulence production  
 270 via  $S_{12}(r, y)$  in the intermediate  $y$ -region (see equation 4.8). Our results on  $\tilde{S}_{12}(r, y)$ ,  
 271  $\tilde{R}_{12}(y, r)$  and  $\tilde{C}_{12}(r, y)$  and their signs carry over qualitatively to  $S_{12}(r, y)$ ,  $R_{12} \equiv$   
 272  $2 \int \langle u_2^+ u_1^+ \rangle [1 - (\frac{r_2}{2y})^2]^{-1} d\Omega_r$  and  $C_{12}(r, y) \equiv 2 \int \langle u_2^+ u_1^- \rangle [1 - (\frac{r_2}{2y})^2]^{-1} d\Omega_r$  (with differences

273 only at values of  $r$  close to  $2y$  because of the factor  $[1 - (\frac{r_2}{2y})^2]^{-1}$  in the integrands which  
 274 tends to infinity for  $r_2 \rightarrow 2y$ , see figures 3(c,d) and 4(c,d) and compare them, respectively,  
 275 with figures 3(a,b) and 4(a,b)). The two-point turbulence production is therefore positive  
 276 for all  $r \leq 2y$  and all  $y$  in the intermediate range mainly because one-point turbulence  
 277 production is positive even though two-point correlations conditioned on aligned fluctu-  
 278 ating velocities act to reduce this positivity. Two-point correlations conditioned on  
 279 anti-aligned fluctuating velocities enhance the positive two-point turbulence production  
 280 particularly at the larger separations  $r$ .

## 281 6. Interscale transfer rate

282 Having analysed the production term in the scale-by-scale turbulence energy balance 4.1  
 283 we now turn our attention to the interscale transfer rate 4.2 and the viscous diffusion  
 284 terms 4.3. We adapt to the scale-by-scale turbulence energy balance 4.9 (which we derived  
 285 from 4.1) the matched asymptotic expansion approach that Lundgren (2002) used to  
 286 study freely decaying homogeneous isotropic turbulence, a very different flow from FD  
 287 TCF.

288 The starting point is the hypothesis that  $S_2$ ,  $S_3$  and  $S_{12}$  have similarity forms, namely

$$289 \quad S_2(r, y) = v^2(y) s_2(r/l(y), y) \quad (6.1)$$

$$290 \quad S_3(r, y) = v^3(y) s_3(r/l(y), y) \quad (6.2)$$

$$291 \quad S_{12}(r, y) = v^2(y) s_{12}(r/l(y), y) \quad (6.3)$$

292 in terms of a characteristic velocity  $v$  and a characteristic length  $l$  both of which depend  
 293 on wall-normal distance  $y$ . In the following two subsections, this hypothesis is made for  
 294 small scales  $r \ll l_o$  in terms of an inner characteristic velocity  $v = v_i$  and an inner  
 295 characterisitic length  $l = l_i$  and is also made for large scales  $r \gg l_i$  in terms of an outer  
 296 characteristic velocity  $v = v_o$  and outer characteristic length  $l = l_o$ .

297 From the one-point balance between average turbulence production  $-\langle u_1 u_2 \rangle \frac{dU_1}{dy}$  and  
 298 average turbulence dissipation in the intermediate range  $\delta_\nu \ll y \ll \delta$  it is classically  
 299 claimed, by assuming validity of the log law for the mean flow and its consequence on  
 300 the one-point Reynolds shear stress, that the turbulence dissipation rate equals  $u_\tau^3/(\kappa y)$   
 301 (e.g. see Pope 2000). Even though there are deviations from both the log law and this  
 302 dissipation scaling (e.g. Dallas *et al.* (2009); Vassilicos *et al.* (2015)), we use here the  
 303 relation  $\varepsilon^v = 4u_\tau^3/(\kappa y)$  as an acceptable approximation (in all figures, however,  $\varepsilon^v$  is  
 304 computed from the numerical data).  
 305  
 306

With  $\varepsilon^v = 4u_\tau^3/(\kappa y)$  and similarity forms 6.1, 6.2 and 6.3, the balance 4.9 becomes

$$\begin{aligned} & \frac{\kappa}{4} \frac{v^3(y)}{u_\tau^3} \frac{s_3(r/l(y))}{r/y} \\ & - \frac{3\kappa y^2}{32\pi r^3 y^+} \int_0^r \rho^2 \frac{d^2 \left[ \frac{v^2(y)}{u_\tau^2} s_2(\rho/l(y)) \right]}{dy^2} d\rho - \frac{3\kappa y^2}{4\pi r y^+} \frac{d}{dr} \left[ \frac{v^2(y)}{u_\tau^2} s_2(r/l(y)) \right] \\ & \approx -1 - \frac{3}{16\pi r^3} \int_0^r \rho^2 \frac{v^2(y)}{u_\tau^2} s_{12}(\rho/l(y)) d\rho \end{aligned} \quad (6.4)$$

308 where  $y^+ \equiv y/\delta_\nu = u_\tau y/\nu$  is a naturally appearing local Reynolds number. The functions  
 309  $s_2$ ,  $s_3$  and  $s_{12}$  have also explicit dependencies on  $y$  in equations (6.4), (6.5) and (6.10)  
 310 which are omitted to lighten notation.

311 In the limit  $y^+ \gg 1$  within the intermediate range  $\delta_\nu \ll y \ll \delta$ , which of course also

312 requires the limit  $Re_\tau = \delta/\delta_\nu \gg 1$ , we consider separately outer similarity with outer  
 313 variables  $v = v_o$  and  $l = l_o$  for  $r \gg l_i$  and inner similarity with inner variables  $v = v_i$   
 314 and  $l = l_i$  for  $r \ll l_o$ .

315

### 6.1. Outer similarity

For  $r$  large enough, i.e.  $r \gg l_i(y)$  (where the inner length-scale  $l_i$  is to be determined), the most natural choice for outer variables is  $v = v_o = u_\tau$  and  $l = l_o = y$  given that the distance to the wall should somehow determine the size of large eddies and that their characteristic velocity should scale with the skin friction velocity. With these outer variables, equation 6.4 becomes

$$\begin{aligned} & \frac{\kappa s_3(r/y)}{4} \frac{r/y}{r/y} \\ & - \frac{3\kappa y^2}{32\pi r^3 y^+} \int_0^r \rho^2 \frac{d^2[s_2(\rho/y)]}{dy^2} d\rho - \frac{3\kappa y^2}{4\pi r y^+} \frac{d}{dr}[s_2(r/y)] \\ & \approx -1 - \frac{3}{16\pi r^3} \int_0^r \rho^2 s_{12}(\rho/y) d\rho \end{aligned} \quad (6.5)$$

317 In the limit  $y^+ \gg 1$ , viscous diffusion (the second and third terms on the left hand side)  
 318 tends to 0 as  $1/y^+$  compared to the other terms. This equation therefore suggests outer  
 319 asymptotic expansions in integer powers of  $\frac{1}{y^+}$ , which means that the outer similarity  
 320 functions  $s_2$ ,  $s_3$  and  $s_{12}$  may be approximated as

$$321 \quad s_2^o(r/y, y^+) = s_2^{o,0} + \frac{1}{y^+} s_2^{o,1} + \dots \quad (6.6)$$

322

$$323 \quad s_3^o(r/y, y^+) = s_3^{o,0} + \frac{1}{y^+} s_3^{o,1} + \dots \quad (6.7)$$

324

$$325 \quad s_{12}^o(r/y, y^+) = s_{12}^{o,0} + \frac{1}{y^+} s_{12}^{o,1} + \dots \quad (6.8)$$

326 with leading orders obeying

$$327 \quad \frac{\kappa s_3^{o,0}(r/y)}{4} \frac{r/y}{r/y} \approx -1 - \frac{3}{16\pi r^3} \int_0^r \rho^2 s_{12}^{o,0}(\rho/y) d\rho. \quad (6.9)$$

328 The leading order outer scale-by-scale energy balance is therefore a balance between inter-  
 329 scale transfer, turbulence dissipation and two-point turbulence production. (Turbulence  
 330 dissipation appears in this outer balance essentially because the scale-by-scale energy  
 331 balance that we consider concerns the sphere-averaged second order structure function  
 332 which is cumulative with increasing  $r$ .)

333

### 6.2. Inner similarity

For  $r$  small enough, i.e.  $r \ll l_o = y$ , we seek inner variables of the form  $v_i^2 = v_o^2(\frac{1}{y^+})^a = u_\tau^2(\frac{1}{y^+})^a$  and  $l_i = l_o(\frac{1}{y^+})^b = y(\frac{1}{y^+})^b$  where the exponents  $a, b$  are positive because inner variables should tend to 0 relative to outer ones in the limit where the local Reynolds

number  $y^+$  tends to infinity. With such variables, equation 6.4 becomes

$$\begin{aligned} & \frac{\kappa}{4} \left( \frac{1}{y^+} \right)^{\frac{3a}{2}-b} \frac{s_3(r/l_i)}{r/l_i} \\ & - O \left[ \left( \frac{1}{y^+} \right)^{a+3-2b} \right] - \frac{3\kappa}{4\pi} \left( \frac{1}{y^+} \right)^{a+1-2b} \frac{s_2'(r/l_i)}{r/l_i} \\ & \approx -1 - \frac{3}{16\pi r^3} \int_0^r \rho^2 \left( \frac{1}{y^+} \right)^a s_{12}(\rho/l_i) d\rho \end{aligned} \quad (6.10)$$

335 where  $s_2'(r/l_i)$  is the derivative of  $s_2$  with respect to  $r/l_i$ . In the limit  $y^+ \gg 1$ , the two-  
 336 point turbulence production rate tends to 0 as  $(1/y^+)^a$  compared to the dissipation rate  
 337 which is represented in this equation by  $-1$  on the right hand side. At inner scales, the  
 338 leading order scale-by-scale turbulence energy balance must therefore involve interscale  
 339 energy transfer and viscous diffusion to balance dissipation, which implies  $\frac{3a}{2}-b=0=a+$   
 340  $1-2b$  and therefore  $a=1/2$  and  $b=3/4$ . In the limit  $y^+ \rightarrow \infty$ , i.e.  $y^+ \gg 1$ , this equation  
 341 therefore suggests inner asymptotic expansions in integer powers of  $(\frac{1}{y^+})^a = (\frac{1}{y^+})^{1/2}$ ,  
 342 which means that the inner similarity functions  $s_2$ ,  $s_3$  and  $s_{12}$  may be approximated as

$$343 \quad s_2^i(r/l_i, y^+) = s_2^{i,0} + \left( \frac{1}{y^+} \right)^{1/2} s_2^{i,1} + \dots \quad (6.11)$$

344

$$345 \quad s_3^i(r/l_i, y^+) = s_3^{i,0} + \left( \frac{1}{y^+} \right)^{1/2} s_3^{i,1} + \dots \quad (6.12)$$

346

$$347 \quad s_{12}^i(r/l_i, y^+) = s_{12}^{i,0} + \left( \frac{1}{y^+} \right)^{1/2} s_{12}^{i,1} + \dots \quad (6.13)$$

348 with leading orders obeying

$$349 \quad \frac{\kappa}{4} \frac{s_3^{i,0}(r/l_i)}{r/l_i} \approx -1 - \frac{3\kappa}{4\pi} s_2^{i,0'}(r/l_i) \quad (6.14)$$

350 where  $s_2^{i,0'}(r/l_i)$  is the derivative of  $s_2^{i,0}$  with respect to  $r/l_i$ . The leading order inner scale-  
 351 by-scale energy balance is therefore a balance between interscale transfer, turbulence  
 352 dissipation and viscous diffusion.

353 The values  $a=1/2$  and  $b=3/4$  that we derived imply that the inner variables are in  
 354 fact Kolmogorov inner variables, i.e.  $v_i = u_\eta \equiv (\nu \varepsilon^v)^{1/4}$  and  $l_i = \eta \equiv (\nu^3/\varepsilon^v)^{1/4}$  (using  
 355  $\varepsilon^v = u_\tau^3/(\kappa y)$ ).

356

### 6.3. Intermediate matching

357 Starting with the second order structure function  $S_2$ , matching the leading term  
 358  $u_\tau^2 s_2^{i,0}(r/y)$  of its outer expansion for  $r \gg \eta$  with the leading term  $u_\tau^2 (\frac{1}{y^+})^{1/2} s_2^{i,0}(r/\eta)$  of  
 359 its inner expansion for  $r \ll y$  leads to

$$360 \quad S_2^0 \sim (\varepsilon^v r)^{2/3} \quad (6.15)$$

361 as overlapping part of the leading order in the intermediate range  $\eta \ll r \ll y$ .

362 Similarly,

$$363 \quad S_{12}^0 \sim (\varepsilon^v r)^{2/3} \quad (6.16)$$

364 is the overlapping part of the leading order in the intermediate range  $\eta \ll r \ll y$  for  $S_{12}$ .

365 It may be interesting to note, in passing, the difference compared to turbulence non-  
 366 homogeneities with negligible turbulence production but non-negligible spatial turbulence

transport such as in certain turbulent wake regions where Chen & Vassilicos (2022) have shown that a second order structure function scales as  $\sim K(r/L)^{2/3}$  where  $K$  is the one-point kinetic energy,  $L$  is an integral length scale, and turbulence dissipation does not scale as  $K^{3/2}/L$ . Note that the  $K^{3/2}/L$  scaling is effectively the scaling assumed here for  $\varepsilon^v$  because, in the range  $\delta_\nu \ll y \ll \delta$  considered here, the turbulent kinetic energy scales as  $u_\tau^2$  plus logarithmic corrections in  $y$  (see Townsend 1976; Dallas *et al.* 2009) which we neglect, and because there are integral length scales in FD TCF which are proportional to  $y$ , see Apostolidis *et al.* (2022). The types of non-homogeneity considered by Chen & Vassilicos (2022) are opposite to the ones considered here where spatial turbulence transport is negligible but turbulence production is not.

To obtain the leading order of  $S_3$ , and therefore of the interscale transfer rate  $\Pi^v$  via equation 4.2, we use equations 6.9 and 6.14. From the leading order outer balance 6.9 follows

$$S_3^{o,0} \approx -\varepsilon^v r(1 - A(r/y)^{2/3}) \quad (6.17)$$

where  $A$  is a dimensionless constant, and from the leading order inner balance 6.14 follows

$$S_3^{i,0} \approx -\varepsilon^v r(1 - B(r/\eta)^{-4/3}) \quad (6.18)$$

where  $B$  is another dimensionless constant. The composite leading order (see Van Dyke 1964; Cole 1968; Hinch 1991) written directly for the interscale transfer  $\Pi^v = S_3/r$  is  $S_3^{o,0}/r$  plus  $S_3^{i,0}/r$  minus their common part  $-\varepsilon^v$ , i.e.

$$\Pi^v \approx -\varepsilon^v(1 - A(r/y)^{2/3} - B(r/\eta)^{-4/3}) \quad (6.19)$$

where we now omit superscripts for ease of notation.

This last equation has the following two verifiable implications, both of which are relatively easy to verify with the DNS data at our disposal: firstly it implies that the value of  $r$  where  $\Pi^v/\varepsilon^v$  is minimal and closest to the Kolmogorov equilibrium value -1 is

$$r_{\min} \sim \sqrt{\delta_\nu y} \sim \lambda \quad (6.20)$$

based on the definition  $\lambda^2 \equiv 10\nu K/\varepsilon$  (already used by Dallas *et al.* (2009) in the context of FD TCF), and on  $K \sim u_\tau^2$  and  $\varepsilon \sim u_\tau^3/y$  being good enough approximations in the present context for  $\delta_\nu \ll y \ll \delta$ . Conclusions such as 6.19 and 6.20 have recently been obtained by Zimmerman *et al.* (2022) for the centreline of FD TCF and central axis of turbulent pipe flow where turbulence production is effectively absent.

Secondly, 6.19 also implies that the value  $(\Pi^v/\varepsilon^v)_{\min}$  of  $\Pi^v/\varepsilon^v$  at  $r = r_{\min}$  obeys

$$1 + (\Pi^v/\varepsilon^v)_{\min} \sim y^{+1/3} \sim Re_\lambda^{-2/3} \quad (6.21)$$

where  $Re_\lambda = \sqrt{K}\lambda/\nu$ . Consistently with our averages over spheres in  $\mathbf{r}$ -space, these definitions of  $\lambda$  and  $Re_\lambda$  ignore some anisotropies of FD TCF. It is possible to define different Taylor lengths for different directions so as to take explicit account of anisotropies, which is an approach we have taken in another study (Yuvaraj 2022). It may be noteworthy that the Corrsin length (Sagaut & Cambon 2018) does not appear spontaneously from our analysis whereas the Kolmogorov and Taylor lengths do. The reason for this absence of the Corrsin length is that it equals  $\kappa y$  at the approximation level of our theory in the intermediate layer  $\delta_\nu \ll y \ll \delta$  and is therefore comparable to the outer bound of the range  $r \leq 2y$  considered here.

In conclusion, the non-homogeneous but statistically stationary case of FD TCF in the intermediate layer  $\delta_\nu \ll y \ll \delta$  is such that Kolmogorov equilibrium is achieved asymptotically around  $\lambda$  and therefore not quite in an inertial range given that  $\lambda$  depends on viscosity and that there is a systematic departure from equilibrium when moving away

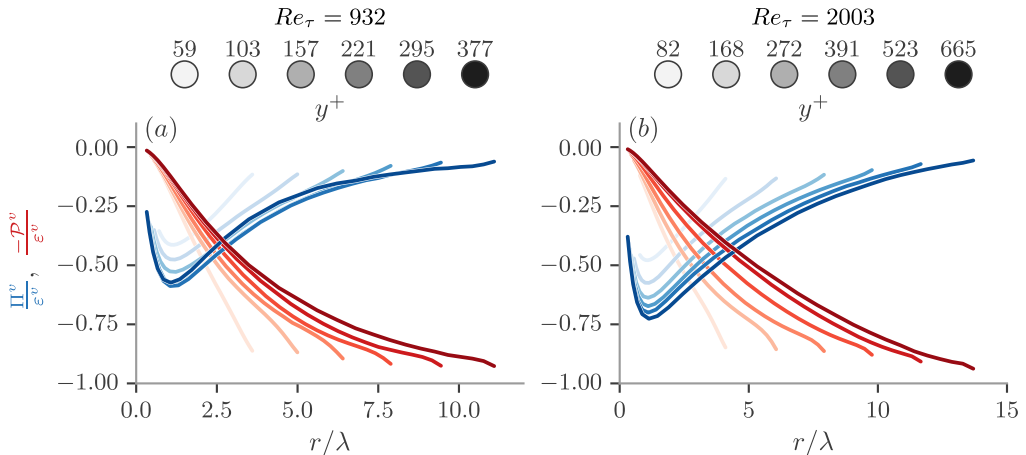


FIGURE 5. Interscale transfer rate  $\Pi$  (blue lines) and production rate  $\mathcal{P}$  (red lines), integrated over the volume of sphere with radius  $r$ , normalised by the volume integral of the two point dissipation rate  $\varepsilon$  as a function of  $r/\lambda$ . Wall-normal distance is increased from light to dark colors. (a) for  $Re_\tau = 932$  and (b) for  $Re_\tau = 2003$ .

412 from  $\lambda$ , both towards  $L$  and towards  $\eta$ , see equation 6.19. (Note, however, that the non-  
 413 zero deviation from Kolmogorov equilibrium as Reynolds number tends to infinity for  
 414 a fixed small value of  $r/y$  or for a fixed large value of  $r/\eta$  (necessarily smaller than  
 415  $\lambda/\eta$  in the limit) is small). This is the same conclusion that the analysis of Lundgren  
 416 (2002) reached for freely decaying, i.e. non-stationary, but statistically homogeneous and  
 417 isotropic turbulence far from initial conditions. Two-point turbulence production (which  
 418 increases with  $r$  as confirmed in the following section) and its variation with wall-normal  
 419 distance play a similar role in FD TCF as the rate of decay of the second order velocity  
 420 structure function (which increases with  $r$  because unsteadiness increases with  $r$ ) and its  
 421 variation with time.

## 422 7. Comparison with DNS data for FD TCF

423 In this section we compare the theory of the previous sections with the DNS data  
 424 described in section 3.

425 In figure 5(a,b) we plot the two-point turbulence production rate  $\mathcal{P}^v$  and the interscale  
 426 transfer rate  $\Pi^v$ , both normalised by the turbulence dissipation rate  $\varepsilon^v$ . We plot them  
 427 versus  $r/\lambda$  because of our prediction that the value of  $r$ , where  $\Pi^v/\varepsilon^v$  is minimal scales  
 428 with  $\lambda$ . The maximum values of  $r$  in the plots are bounded by  $2y$  because of wall-blocking.  
 429 We see that the normalised two-point turbulence production rate  $\mathcal{P}^v/\varepsilon^v$  increases from  
 430 close to 0 to a little under 1 as  $r$  increases from 0 to  $2y$ . This is evidenced for a wide range  
 431 of wall-normal distances  $y$  and for both Reynolds numbers at our disposal. It makes sense  
 432 that the two-point turbulence production acts as a generation of turbulent kinetic energy  
 433 at the larger  $r$  scales but decreasingly so at smaller and smaller scales till it vanishes at  
 434 the very smallest ones.

435 It is also clear from figure 5(a,b) that  $\Pi^v$  is negative for all scales and wall-distances,  
 436 indicating a forward, on average, energy cascade for  $r < 2y$ . Furthermore,  $\Pi^v/\varepsilon^v$  has a  
 437 minimum at  $r_{\min}$  close to  $\lambda$  for a wide range of  $y$  within  $\delta_\nu \ll y \ll \delta$  and for both Reynolds  
 438 numbers. This confirms our prediction 6.20 as can be seen in figure 6(a) where we plot,  
 439 in blue,  $r_{\min}/\lambda$  versus  $y^+$  for both Reynolds numbers and find that  $r_{\min} \approx 1.2\lambda$ . One also

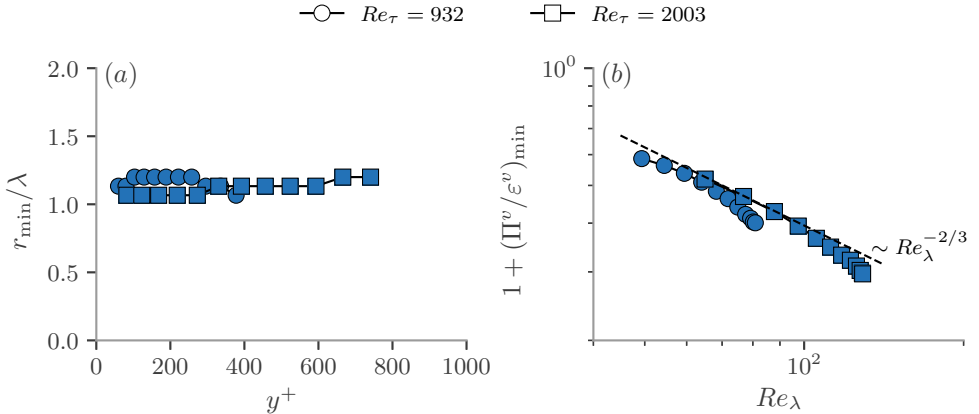


FIGURE 6. (a) Values of  $r/\lambda$  where minima of  $\Pi^v/\varepsilon^v$  are observed as function of wall distance  $y^+$ . (b) Values of  $1 + (\Pi^v/\varepsilon^v)_{\min}$  in blue, as a function of  $Re_\lambda$ . Dashed line shows a scaling of  $Re_\lambda^{-2/3}$ . Circle markers for  $Re_\tau = 932$ , Square markers for  $Re_\tau = 2003$ .

440 sees in figure 5(a,b) that  $(\Pi^v/\varepsilon^v)_{\min}$  increases in magnitude with increasing  $y^+$  and with  
 441 increasing  $Re_\tau$ . This is confirmed in figure 6(b) where we plot, in blue,  $1 + (\Pi^v/\varepsilon^v)_{\min}$   
 442 versus  $Re_\lambda$  confirming that  $-(\Pi^v/\varepsilon^v)_{\min}$  increases towards 1 following our prediction  
 443 6.21 which collapses both the  $y^+$  and the  $Re_\tau$  dependencies of  $-(\Pi^v/\varepsilon^v)_{\min}$ . Note, in  
 444 passing, that the values of  $Re_\lambda$  are not so high for the present  $Re_\tau$  values of about 1000  
 445 to 2000: they range from about 50 to 120 (and in fact reach no more than maximum 200  
 446 at the outer edge of the intermediate  $y$ -range if  $Re_\tau$  is pushed up to 5200 as one can find  
 447 in Apostolidis *et al.* (2022)).

448 The imbalance seen in figure 5 between  $\Pi^v$  and  $\varepsilon^v$  is clear indication that other  
 449 processes in the scale-by-scale energy budget are active. The theoretical arguments  
 450 of subsections 6.1 and 6.2 concluded that the scale-by-scale balance is approximately  
 451  $\Pi^v - \mathcal{P}^v \approx -\varepsilon^v$  at the outer scales and  $\Pi^v - D_r^v \approx -\varepsilon^v$  at the inner scales. This  
 452 prediction is made in the limit  $Re_\tau = \delta/\delta_\nu \gg 1$  and  $\delta_\nu \ll y \ll \delta$  and, as the values  
 453 of  $Re_\lambda$  suggest, the Reynolds numbers in the DNS data we are using may not be high  
 454 enough. Nevertheless, figure 7(a, b) does reveal some tendency for  $(\Pi^v - \mathcal{P}^v)/\varepsilon^v$  to collapse  
 455 as a function of  $r/y$  and tend towards  $-1$  at the higher values of  $r/y$  as  $y^+$  grows, in  
 456 particular for the higher of our two Reynolds numbers  $Re_\tau$ . Furthermore, figure 7(c, d)  
 457 reveals some tendency for  $(\Pi^v - D_r^v)/\varepsilon^v$  to collapse as a function of  $r/\eta$  as  $y^+$  grows and  
 458 even to tend towards  $-1$  at the smallest values of  $r/\eta$ .

459 Finally, we compare the high Reynolds number predictions 6.15, 6.16 and 6.19 with  
 460 the DNS data. In figure 8(a, b) we plot  $S_2/u_\tau^2(r/y)^{2/3}$  and  $S_{12}/u_\tau^2(r/y)^{2/3}$  versus  $r/y$   
 461 to test outer scalings and in figure 8(c, d) we plot the same quantities versus  $r/\eta$  to  
 462 test inner scalings. Note that we use  $u_\tau^3/y$  as an estimate of  $\varepsilon^v$ . Our DNS data lend  
 463 more support to our  $r^{2/3}$  prediction for  $S_{12}$  than for  $S_2$ , and a better outer collapse in  
 464 terms of  $r/y$  of  $S_{12}/u_\tau^2(r/y)^{2/3}$  than  $S_2/u_\tau^2(r/y)^{2/3}$ . However the inner collapse in terms  
 465 of  $r/\eta$  appears better for  $S_2/u_\tau^2(r/y)^{2/3}$  than  $S_{12}/u_\tau^2(r/y)^{2/3}$ . At any rate, the values  
 466 of  $Re_\lambda$  are quite low in the DNS data used here for a conclusive comparison between  
 467 these data and theoretical predictions made in the double limit  $Re_\tau \rightarrow \infty$ ,  $y^+ \rightarrow \infty$   
 468 (i.e.  $Re_\lambda \sim \lambda/\delta_\nu \sim (y^+)^{1/2} \rightarrow \infty$ ) with the constraint  $y \ll \delta$ . In fact, even at the  
 469 very lowest/leading order, our predictions 6.15, 6.16 are incomplete as they should have

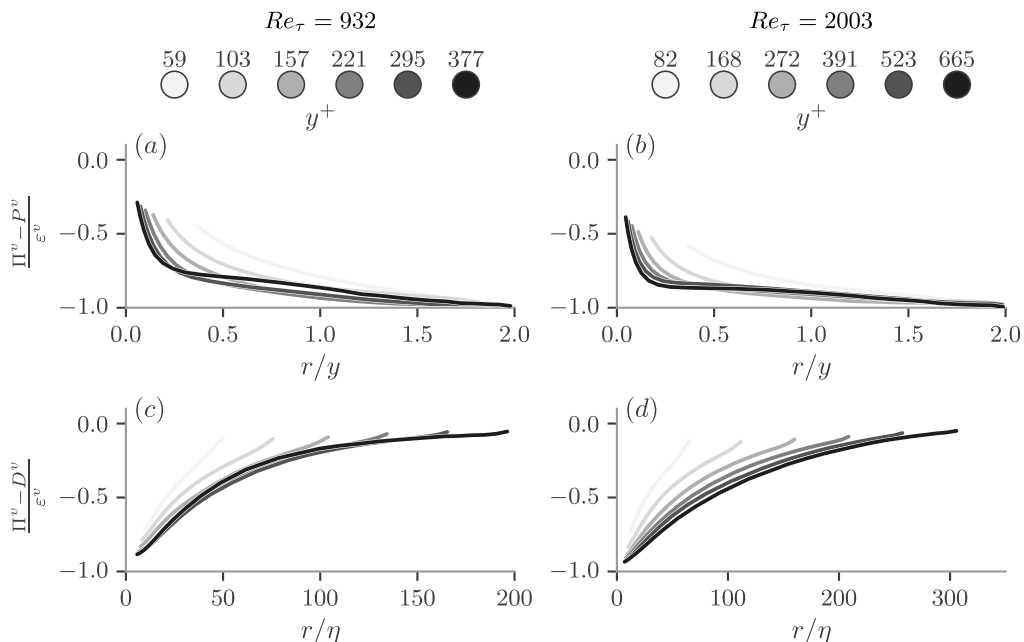


FIGURE 7. (a, b)  $(II^v - \mathcal{P}^v)/\varepsilon^v$  as a function of  $r/y$ . (a) for  $Re_\tau = 932$  and (b) for  $Re_\tau = 2003$ . (c, d)  $(II^v - D^v)/\varepsilon^v$  as a function of  $r/\eta$  for  $Re_\tau = 932$  in (c) and  $Re_\tau = 2003$  in (d). Wall-normal distance is increased from light to dark colors.

470 corrections in terms of powers of  $r/\eta$  and  $r/y$  which are beyond the present theory and  
 471 which surely matter in comparisons with DNS data.

472 We close this section with a comparison in figure 9 of 6.19 with the DNS data which  
 473 is clearly better for  $Re_\tau = 2003$  than  $Re_\tau = 932$ .

## 474 8. Interscale transfer decompositions

475 The two main conclusions of the previous sections concern (i) the importance of the  
 476 Taylor length in defining the scale where the normalised interscale transfer rate  $II^v/\varepsilon^v$  has  
 477 a minimum and is closest to the equilibrium value  $II^v/\varepsilon^v = -1$  and (ii) the importance  
 478 of sweeps and ejections but also of aligned and anti-aligned pairs of fluctuating velocities  
 479 in determining the sign and magnitude of the two-point turbulence production rate  $\mathcal{P}^v$ .  
 480 Looking at equation 4.2, we start this section by asking whether aligned and anti-aligned  
 481 pairs of fluctuating velocities also directly affect the interscale transfer rate  $II^v$ .

482

### 8.1. Aligned/anti-aligned decomposition

483 Equation 4.2 shows that a scale-space flux and a cascade from large to small or from small  
 484 to large scales correspond to a negative or positive  $\frac{3}{4\pi} \int \langle \frac{\hat{\mathbf{r}} \cdot \partial \mathbf{u}}{r} |\delta \mathbf{u}|^2 \rangle d\Omega_{\hat{\mathbf{r}}}$  and contributes  
 485 a growth or decrease of TKE at scales  $r$  and smaller (see Chen & Vassilicos 2022). Local  
 486 compression, i.e.  $\delta \mathbf{u} \cdot \hat{\mathbf{r}} < 0$ , causes local forward cascade and local stretching, i.e.  $\delta \mathbf{u} \cdot \hat{\mathbf{r}} > 0$ ,  
 487 causes local inverse cascade. Our observation that  $II^v$  is negative at all scales means that  
 488 local compressions prevail at all scales, but are they mostly caused by aligned or anti-  
 489 aligned pairs of fluctuating velocities? This question introduces our first decomposition,



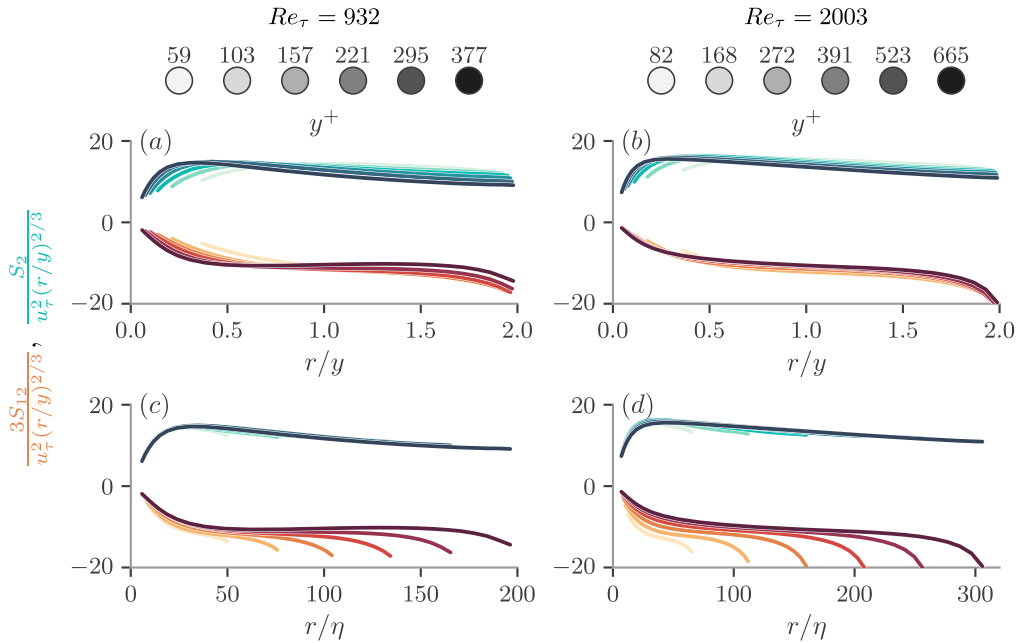


FIGURE 8.  $S_{12}$  in orange colors (multiplied by a factor of 3 for ease of comparison) and  $S_2$  in marine colors normalised with  $u_\tau^2(r/y)^{2/3}$  as a function of  $r/y$  in the first row (a, b) and of  $r/\eta$  in second row (c, d). Left column (a, c) is for  $Re_\tau = 932$ , right column (b, d) is for  $Re_\tau = 2003$ . Wall-normal distance is increased from light to dark colors.

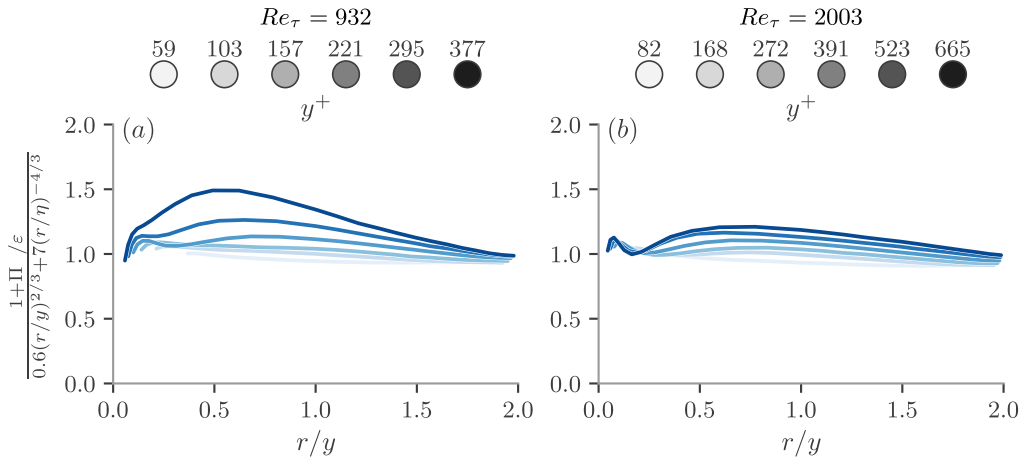


FIGURE 9. Rearrangement of equation 6.19 versus  $r/y$ . (a) for  $Re_\tau = 932$ , (b) for  $Re_\tau = 2003$ . Wall-normal distance is increased from light to dark colors.

490 namely

$$491 \quad \Pi^v = \Pi_{\Rightarrow}^v + \Pi_{\Leftarrow}^v = \frac{3}{4\pi} \int \left\langle \frac{\delta \mathbf{u} \cdot \hat{\mathbf{r}}}{r} |\delta \mathbf{u}|^2 \right\rangle_{\Rightarrow} d\Omega_r + \frac{3}{4\pi} \int \left\langle \frac{\delta \mathbf{u} \cdot \hat{\mathbf{r}}}{r} |\delta \mathbf{u}|^2 \right\rangle_{\Leftarrow} d\Omega_r \quad (8.1)$$

492 where  $\Pi_{\Rightarrow}^v$  and  $\Pi_{\Leftarrow}^v$  are respectively equal to the first and second terms on the left hand  
 493 side which are calculated using averages  $\langle \dots \rangle_{\Rightarrow}$  conditional on  $\mathbf{u}^+ \cdot \mathbf{u}^- > 0$  and averages  
 494  $\langle \dots \rangle_{\Leftarrow}$  conditional on  $\mathbf{u}^+ \cdot \mathbf{u}^- < 0$ .

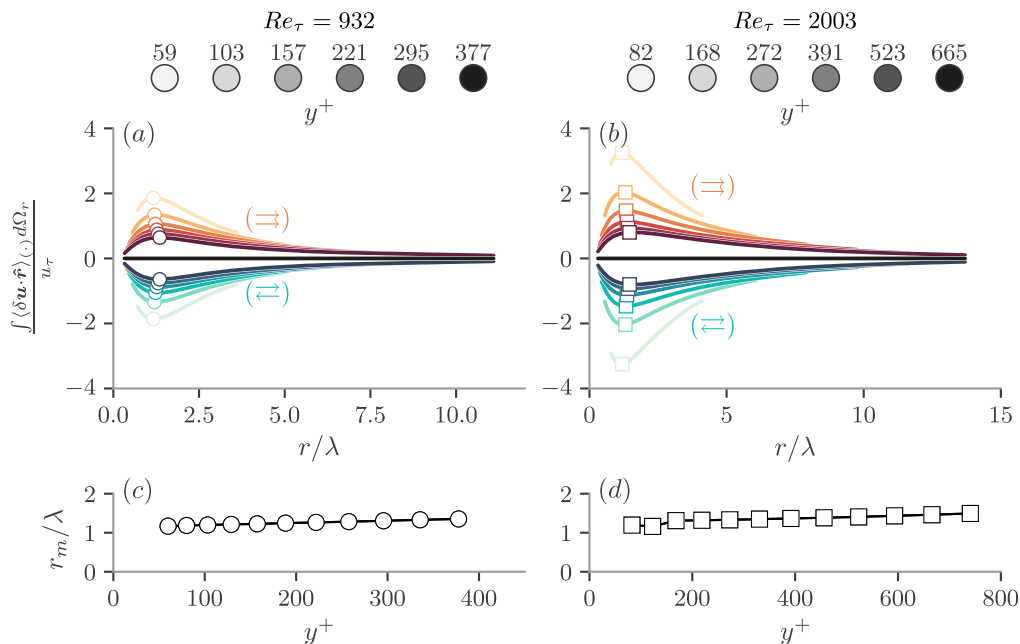


FIGURE 10.  $\int \langle \delta \mathbf{u} \cdot \hat{\mathbf{r}} \rangle d\Omega_r$  integrated over the whole sphere in black lines, conditionally integrated over anti-aligned pairs in marine colors, and conditionally integrated over aligned pairs in orange colors. Wall-normal distance is increased from light to dark colors. (a)  $Re_\tau = 932$ , (b)  $Re_\tau = 2003$ . (c)  $r/\lambda$  positions of the minima/maxima observed in (a) as a function of wall-distance  $y^+$  for  $Re_\tau = 932$ , similarly in (d) for  $Re_\tau = 2003$ .

495 Compressive and stretching relative motions may not balance in terms of energy  
 496 transfer, resulting in a non-vanishing  $\Pi^v$ , but they do balance in terms of mass transfer  
 497 because of incompressibility which implies  $\int \delta \mathbf{u} \cdot \hat{\mathbf{r}} d\Omega_r = 0$ . Hence,

$$498 \int \langle \delta \mathbf{u} \cdot \hat{\mathbf{r}} \rangle_{\Rightarrow} d\Omega_r + \int \langle \delta \mathbf{u} \cdot \hat{\mathbf{r}} \rangle_{\Leftarrow} d\Omega_r = 0 \quad (8.2)$$

499 In figure 10 we plot both terms on the left hand side of this equation as functions of  
 500  $r$  for various wall distances  $y$ . We also plot  $\int \delta \mathbf{u} \cdot \hat{\mathbf{r}} d\Omega_r$  for comparison and as a check  
 501 that it is indeed zero in the DNS irrespective of  $r$  and  $y$ . The first observation is that  
 502 aligned fluctuation pairs are stretching relative motions on average given the positive  
 503 sign of  $\int \langle \delta \mathbf{u} \cdot \hat{\mathbf{r}} \rangle_{\Rightarrow} d\Omega_r$ . The joint PDFs of figure 11 show that relative motions of aligned  
 504 fluctuation pairs are stretching as a result of  $\delta \mathbf{u}$  having a tendency to be directed in  
 505 the same direction as the separation vector  $\mathbf{r}$  for pairs of aligned fluctuating velocities.  
 506 This tendency weakens with increasing  $r$  irrespective of wall distance  $y$  and, consistently,  
 507  $\int \langle \delta \mathbf{u} \cdot \hat{\mathbf{r}} \rangle_{\Rightarrow} d\Omega_r$  tends to 0 with increasing  $r$ .

508 The second observation in figure 10 is that anti-aligned fluctuation pairs are compressing  
 509 relative motions on average given the negative sign of  $\int \langle \delta \mathbf{u} \cdot \hat{\mathbf{r}} \rangle_{\Leftarrow} d\Omega_r$ . Looking at  
 510 figure 11 it does not seem possible to explain this behaviour purely in terms of velocity  
 511 directions. However, the joint PDFs of figure 12 reveal that the range of values over  
 512 which  $\delta \mathbf{u} \cdot \hat{\mathbf{r}}$  fluctuates around zero is much wider for anti-aligned than for aligned  
 513 fluctuations. This effect has to do with the intensity of the fluctuating velocities, not  
 514 only their relative directions. This very wide fluctuation range is slightly skewed towards  
 515 negative values of  $\delta \mathbf{u} \cdot \hat{\mathbf{r}}$  for pairs of fluctuating velocities which are anti-aligned, thereby  
 516 accounting for the compressive average behaviour of anti-aligned pairs ( $\mathbf{u}^+ \cdot \mathbf{u}^- < 0$ ). This

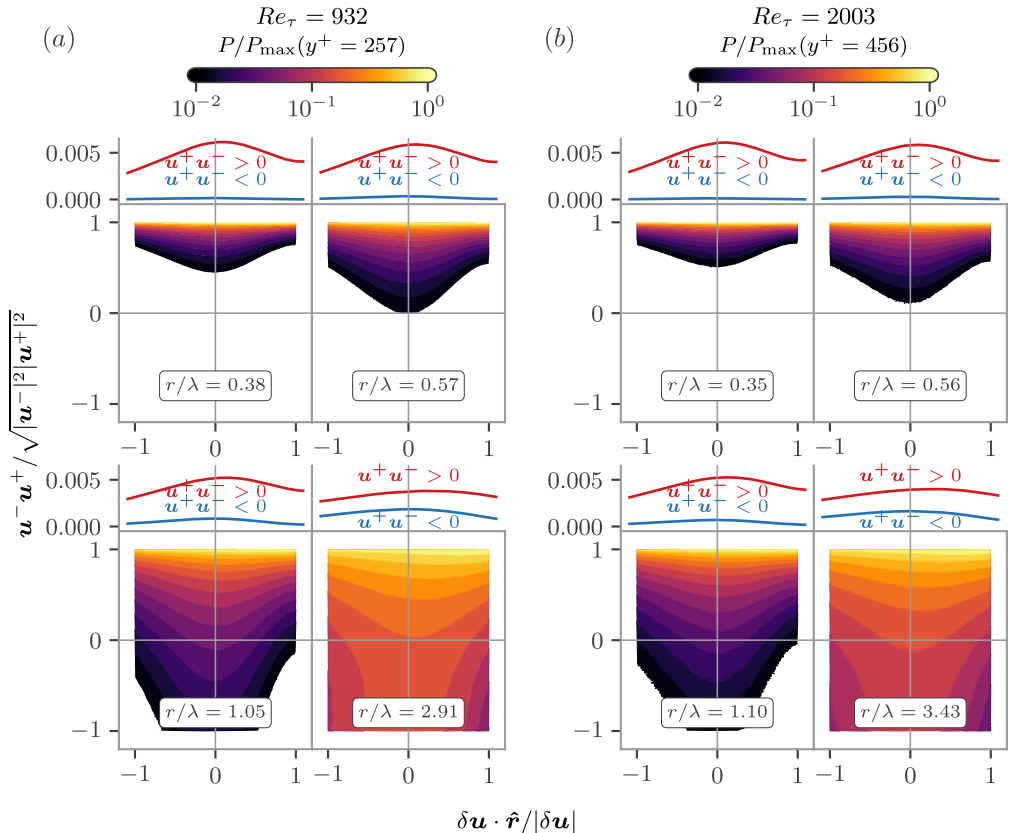


FIGURE 11. Joint probability distribution functions (JPDFs) of  $\delta \mathbf{u} \cdot \hat{\mathbf{r}}/|\delta \mathbf{u}|$  and  $\mathbf{u}^- \mathbf{u}^+ / \sqrt{|\mathbf{u}^+|^2 |\mathbf{u}^-|^2}$ . (a) For  $Re_\tau = 932$  and wall-distance  $y^+ = 257$ , four different JPDFs with increasing scale  $r/\lambda = 0.38, 0.57, 1.05$  and  $2.91$ . (b) Similarly for  $Re_\tau = 2003$  and wall-distance  $y^+ = 456$ , the JPDFs correspond to scales  $r/\lambda = 0.35, 0.56, 1.10$  and  $3.43$ . The joint PDFs are normalised with their maximum value. Above each JPDF, we also plot the conditional PDF of  $\delta \mathbf{u} \cdot \hat{\mathbf{r}}/|\delta \mathbf{u}|$ , conditioned on aligned (red lines) and anti-aligned (blue lines) pairs.

517 skewness diminishes with increasing  $r$  irrespective of wall distance  $y$  and, consistently,  
 518  $\int \langle \delta \mathbf{u} \cdot \hat{\mathbf{r}} \rangle_{\Rightarrow} d\Omega_r$  tends to 0 with increasing  $r$ . Note, finally, that it is far more likely to find  
 519 aligned ( $\mathbf{u}^+ \cdot \mathbf{u}^- > 0$ ) than anti-aligned ( $\mathbf{u}^+ \cdot \mathbf{u}^- < 0$ ) pairs as figure 11 shows.

520 The third observation in figure 10 is that  $\int \langle \delta \mathbf{u} \cdot \hat{\mathbf{r}} \rangle_{\Rightarrow} d\Omega_r$  has a minimum at  $r = r_m$   
 521 near  $r_{\min} \approx 1.2\lambda$  for all  $y$  and that  $\int \langle \delta \mathbf{u} \cdot \hat{\mathbf{r}} \rangle_{\Leftarrow} d\Omega_r$  has a maximum at the same value  
 522  $r = r_m$  for all  $y$ . As seen in the previous two sections,  $r_{\min}$  is the value of  $r$  where  $\Pi^v/\varepsilon^v$   
 523 has its minimum. In figures 10(c, d) we plot the positions  $r$  of the maxima and minima in  
 524 figure 10 versus wall distance for both DNS Reynolds numbers at our disposal. It is quite  
 525 striking that, for all wall distances and both Reynolds numbers tried,  $\int \langle \delta \mathbf{u} \cdot \hat{\mathbf{r}} \rangle_{\Leftarrow} d\Omega_r$  and  
 526  $\int \langle \delta \mathbf{u} \cdot \hat{\mathbf{r}} \rangle_{\Rightarrow} d\Omega_r$  peak at  $r = r_m$  close to the value  $r = r_{\min}$  where  $\Pi^v/\varepsilon^v$  peaks and is  
 527 closest to the equilibrium  $-1$  value. Even though  $r_m$  drifts slightly from  $r_{\min} \approx 1.2\lambda$  at  
 528 relatively high wall-normal distances, the suggestion is that, in the layer  $\delta_\nu \ll y \ll \delta$  of  
 529 FD TCF, Kolmogorov-like equilibrium may be achieved at those length scales  $r$  where  
 530 aligned fluctuating velocities are stretching with their difference  $\delta \mathbf{u}$  maximally or near-  
 531 maximally aligned with the separation vector  $\mathbf{r}$  and where anti-aligned fluctuations are  
 532 maximally or near-maximally skewed towards large negative values of  $\delta \mathbf{u} \cdot \hat{\mathbf{r}}$ . This is

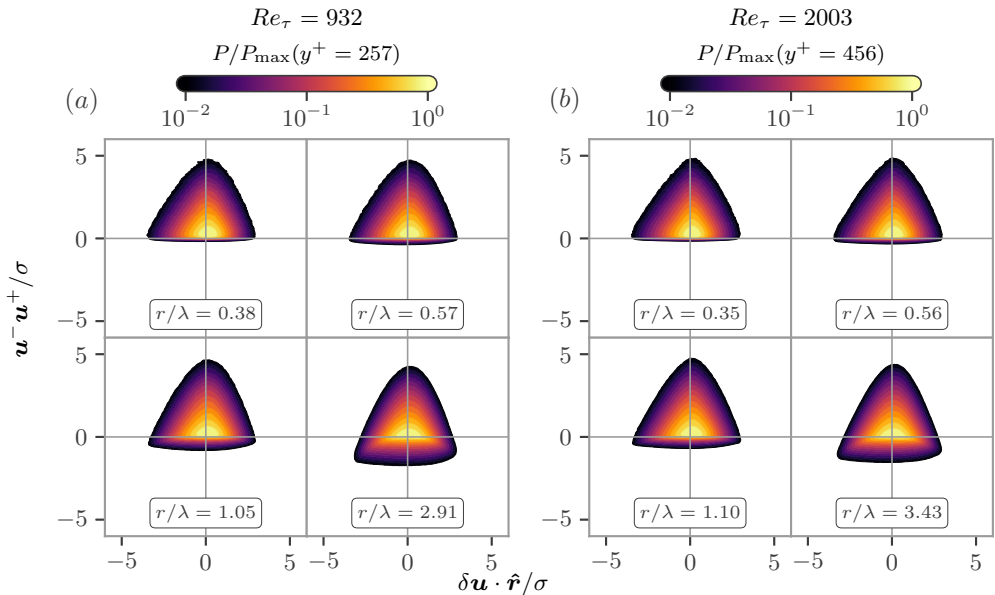


FIGURE 12. Joint probability distribution functions (JPDFs) of  $\delta \mathbf{u} \cdot \hat{\mathbf{r}}$  and  $\mathbf{u}^- \mathbf{u}^+$ . (a) For  $Re_\tau = 932$  and wall-distance  $y^+ = 257$ , four different JPDFs with increasing scale  $r/\lambda = 0.38, 0.57, 1.05$  and  $2.91$ . (b) Similarly for  $Re_\tau = 2003$  and wall-distance  $y^+ = 456$ , the JPDFs correspond to scales  $r/\lambda = 0.35, 0.56, 1.10$  and  $3.43$ . The joint PDFs are normalised with their maximum value, while the values of  $x$  and  $y$  axis are normalised with their own standard deviations.

533 a conclusion that is well beyond the reach of the theory in section 6 but which we  
 534 might not have been able to reach without it. (We refer to Kolmogorov-like rather than  
 535 Kolmogorov equilibrium because the scale  $r_{\min}$  is proportional to the Taylor scale and  
 536 therefore depends on viscosity.)

537 It is shown in section 5 that anti-aligned fluctuation pairs enhance the positive two-  
 538 point turbulence production rate in the layer  $\delta_\nu \ll y \ll \delta$  of FD TCF: we have now seen  
 539 that these anti-aligned fluctuation pairs are on average compressive and figure 13 shows  
 540 that  $\Pi_{\pm}^v$  is consistently negative, indicating forward cascade. Therefore, anti-aligned  
 541 fluctuations do not only enhance two-point production rate at all  $r$ , they also contribute  
 542 a forward cascade at all  $r$  in the layer  $\delta_\nu \ll y \ll \delta$  of FD TCF. Note, however, that the  
 543 minimum value of  $\Pi_{\pm}^v$  is not at  $r = r_{\min}$  where  $\Pi^v/\varepsilon^v$  has its minimum value and is  
 544 closest to the equilibrium  $-1$  value. In fact the  $r$ -position of the minimum value of  $\Pi_{\pm}^v$   
 545 does not scale with  $\lambda$ . The scaling of  $r_{\min}$  therefore requires taking into account both  
 546 aligned and anti-aligned fluctuations.

547 Aligned fluctuation pairs impose a loss of energy on scales smaller than  $r$  by mean flow  
 548 interaction with turbulence fluctuations and thereby reduce the one-point effect of sweeps  
 549 and ejections on the two-point turbulence production rate (see section 5). We have now  
 550 seen that aligned fluctuation pairs are on average stretching, which would suggest the  
 551 presence of an average inverse cascade element to the interscale transfer rate  $\Pi_{\pm}^v$ . Figure  
 552 13 shows that  $\Pi_{\pm}^v$  is positive (though only slightly so), and an average inverse cascade by  
 553 aligned fluctuations is indeed present at scales  $r$  larger than about 2 to 3 times  $\lambda$  for the  
 554 Reynolds numbers of the DNS data used here. However, figure 13 also shows that  $\Pi_{\pm}^v$  is  
 555 negative at smaller scales. Stretching aligned fluctuating motions at scales of the order of  
 556 the Taylor length and below may dominate over compressive aligned fluctuating motions

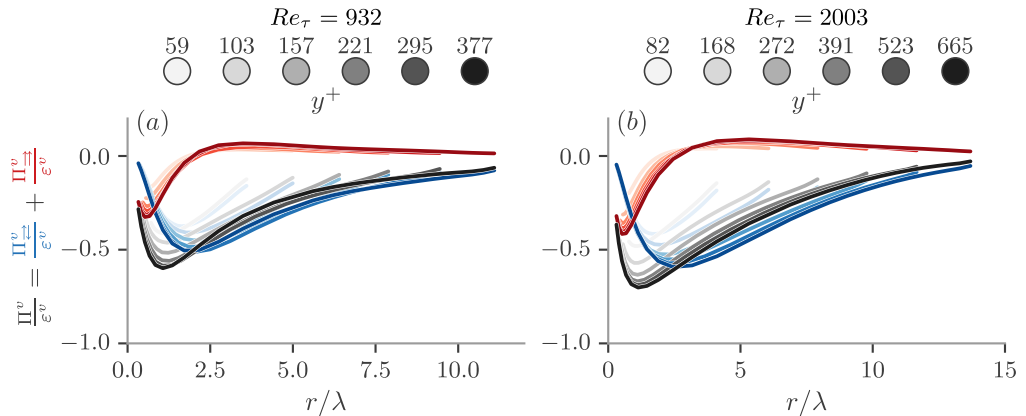


FIGURE 13. Decomposition of the interscale transfer term  $\Pi^v$  (black lines) into  $\Pi_{\u2192}^v$  (blue lines) and  $\Pi_{\u2193}^v$  (red lines). (a)  $Re_\tau = 932$ , (b)  $Re_\tau = 2003$ . Wall-normal distance is increased from light to dark colors.

557 on average but they do not dominate interscale energy transfer at these scales. There is  
 558 no contradiction with the positive values of  $\int \langle \delta \mathbf{u} \cdot \hat{\mathbf{r}} \rangle_{\u2192} d\Omega_r$  in figure 10. The different  
 559 signs of this solid angle integral and the solid angle integral in the definition of  $\Pi_{\u2192}^v$   
 560 (see equation 8.1) are an effect of small-scale anisotropies which we are averaging over.  
 561 Future studies of interscale transfers in FD TCFs will need to take these anisotropies  
 562 into account for a finer description of the physics.

563 Finally, comparing the plots of  $\Pi^v$  in figure 5 with those of  $\Pi_{\u2192}^v$  and  $\Pi_{\u2193}^v$  in figure  
 564 13 shows that  $\Pi_{\u2192}^v$  dominates over  $\Pi_{\u2193}^v$  at scales of the order of  $\lambda$  and larger and is  
 565 mostly responsible for the value of  $\Pi^v$ . At smaller scales, however,  $\Pi_{\u2192}^v$  becomes equally  
 566 important and of the same negative sign as  $\Pi_{\u2193}^v$  so that the actual negative value of  
 567  $\Pi^v$  cannot be accounted for by only one or the other: the interscale turbulence energy  
 568 transfers of both aligned and anti-aligned fluctuations matter.

## 569 8.2. Homogeneous/Inhomogeneous energy transfer decomposition

570 As already mentioned at the start of sub-section 8.1, the right hand side  $\frac{3}{4\pi} \int \langle \hat{\mathbf{r}} \cdot \delta \mathbf{u} \rangle |\delta \mathbf{u}|^2 d\Omega_r$   
 571 of equation 4.2 shows that local compression, i.e.  $\delta \mathbf{u} \cdot \hat{\mathbf{r}} < 0$ , causes local forward cascade  
 572 whereas local stretching, i.e.  $\delta \mathbf{u} \cdot \hat{\mathbf{r}} > 0$ , causes local inverse cascade (see also section 2  
 573 of Chen & Vassilicos (2022)). These compressions and stretches may be caused either by  
 574 turbulence inhomogeneities or by correlated ‘‘eddy’’ motions. In an attempt to formalise  
 575 this distinction, Alves Portela *et al.* (2020) decomposed the interscale energy transfer  
 576 rate  $\Pi = \frac{\partial}{\partial r_i} (\delta u_i |\delta \mathbf{u}|^2)$  as follows:

$$577 \quad \frac{\partial}{\partial r_i} (\delta u_i |\delta \mathbf{u}|^2) = \frac{\partial}{\partial r_i} [\delta u_i (|\mathbf{u}^+|^2 + |\mathbf{u}^-|^2)] - 2 \frac{\partial}{\partial r_i} (\delta u_i \mathbf{u}^- \cdot \mathbf{u}^+) \quad (8.3)$$

578 where the first term on the right hand side can be rigorously recast into a gradient in  
 579 centroid  $\mathbf{x}$ -space leading to

$$\frac{\partial}{\partial r_i} (\delta u_i |\delta \mathbf{u}|^2) = \frac{1}{2} \frac{\partial}{\partial x_i} [u_i^+ |\mathbf{u}^+|^2 + u_i^- |\mathbf{u}^-|^2 - u_i^- |\mathbf{u}^+|^2 - u_i^+ |\mathbf{u}^-|^2] - 2 \frac{\partial}{\partial r_i} (\delta u_i \mathbf{u}^- \cdot \mathbf{u}^+). \quad (8.4)$$

580  $\Pi_I \equiv \frac{1}{2} \frac{\partial}{\partial x_i} [u_i^+ |\mathbf{u}^+|^2 + u_i^- |\mathbf{u}^-|^2 - u_i^- |\mathbf{u}^+|^2 - u_i^+ |\mathbf{u}^-|^2]$  is interpreted as an inhomogeneity-  
 581 related interscale turbulent energy transfer rate. In statistically homogeneous turbulence,  
 582

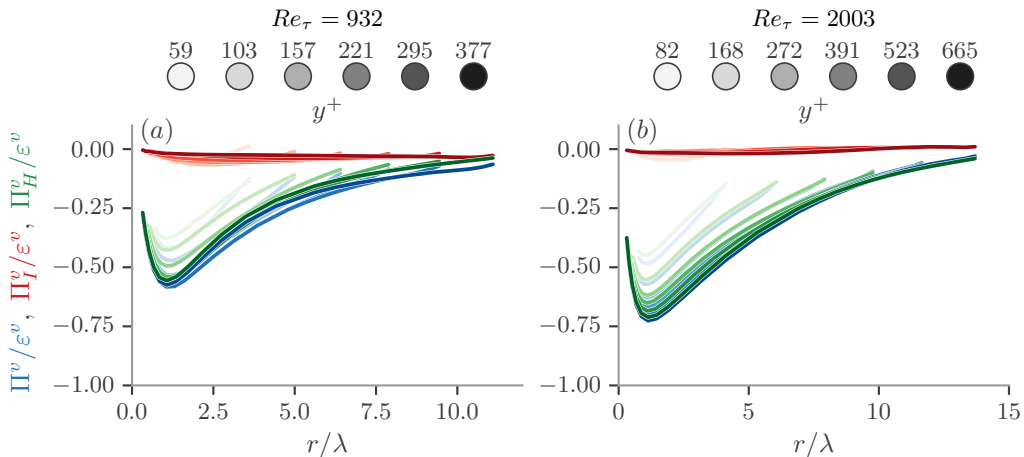


FIGURE 14. Interscale transfer rate (blue lines), inhomogeneous part  $\Pi_I^v$  (red lines), and homogeneous part  $\Pi_H^v$  (green lines), all integrated over the volume of sphere and normalised by the dissipation rate integrated over the volume of the sphere as a function of  $r/\lambda$ . Wall-normal distance is increased from light to dark colors. (a) for  $Re_\tau = 932$  and (b) for  $Re_\tau = 2003$ .

583 the average  $\langle \Pi_I \rangle$  is indeed zero and the interscale turbulent energy transfer rate is only  
 584 accountable to  $\Pi_H \equiv -2 \frac{\partial}{\partial r_i} (\delta u_i \mathbf{u}^- \cdot \mathbf{u}^+)$  on average.

585 Integrating  $\Pi$ ,  $\Pi_I$  and  $\Pi_H$  over the sphere of radius  $r$  in  $\mathbf{r}$ -space to obtain  $\Pi^v$ ,  $\Pi_I^v$   
 586 and  $\Pi_H^v$  respectively and then applying the Gauss divergence theorem we obtain

$$\Pi^v = \Pi_I^v + \Pi_H^v = \frac{3}{4\pi} \left( \int \left\langle \frac{\delta \mathbf{u} \cdot \hat{\mathbf{r}}}{r} (|\mathbf{u}^+|^2 + |\mathbf{u}^-|^2) \right\rangle d\Omega_r - 2 \int \left\langle \frac{\delta \mathbf{u} \cdot \hat{\mathbf{r}}}{r} (\mathbf{u}^- \cdot \mathbf{u}^+) \right\rangle d\Omega_r \right). \quad (8.5)$$

587  
 588 This decomposition is partly related to the one of sub-section 8.1 because  $\Pi_H^v$  is linearly  
 589 dependent on correlations between  $\delta \mathbf{u} \cdot \hat{\mathbf{r}}$  and  $\mathbf{u}^- \cdot \mathbf{u}^+$ , and the sign of  $\mathbf{u}^- \cdot \mathbf{u}^+$  indicates  
 590 whether velocity fluctuation pairs are aligned or anti-aligned which is the basis of  
 591 decomposition 8.1. Whilst it follows immediately from equation 8.4 that  $\Pi_I^v = 0$  if the  
 592 term inside the  $\mathbf{x}$ -gradient in that equation is statistically homogeneous, equation 8.5  
 593 shows that  $\Pi_I^v = 0$  if  $\delta \mathbf{u} \cdot \hat{\mathbf{r}}$  and  $(|\mathbf{u}^+|^2 + |\mathbf{u}^-|^2)$  are uncorrelated and if  $(|\mathbf{u}^+|^2 + |\mathbf{u}^-|^2)$   
 594 is statistically homogeneous. Of course this is not the only and necessary way for  $\Pi_I^v$  to  
 595 vanish. In particular, there may be cases of non-homogeneity for which  $\Pi_I^v$  vanishes too,  
 596 for example cases where  $\Pi_I^v$  vanishes but  $\Pi_H^v$  does not.

597 In figure 14 we plot the terms  $\Pi_I^v$  and  $\Pi_H^v$  in 8.5 normalised by the volume integral  
 598 of the dissipation. For both Reynolds numbers, we observe that  $\Pi_H^v$  dominates and  
 599 describes almost perfectly the full interscale transfer  $\Pi^v$  for all scales  $r \leq 2y$  in the  
 600 intermediate range of the channel ( $y$  between multiples of  $\delta_\nu$  and about half  $\delta$ ). The  
 601 average interscale transfer from large to small scales is nearly fully described by the  
 602 negative value of  $\Pi_H^v$  and the inhomogeneity-related interscale transfer rate  $\Pi_I^v$  is close  
 603 to zero. In a different non-homogenous turbulent flow, the turbulent wake of a square  
 604 prism, Alves Portela *et al.* (2020) found a significant contribution of the inhomogeneity-  
 605 related interscale transfer rate to the total interscale transfer rate. It is therefore not  
 606 trivial that in FD TCF  $\Pi_I^v$  is negligible compared to  $\Pi_H^v$  in spite of the statistical non-  
 607 homogeneity of the FD TCF. However, this is partly an artifact of the integration over  
 608 spheres in  $\mathbf{r}$ -space which we apply to  $\Pi_I$  to obtain  $\Pi_I^v$ . If we lift this integration and use  
 609 the DNS data to compute  $\Pi_I(y, r_1, r_2, r_3)$  as a function of  $r_2/y$  for various values of wall-

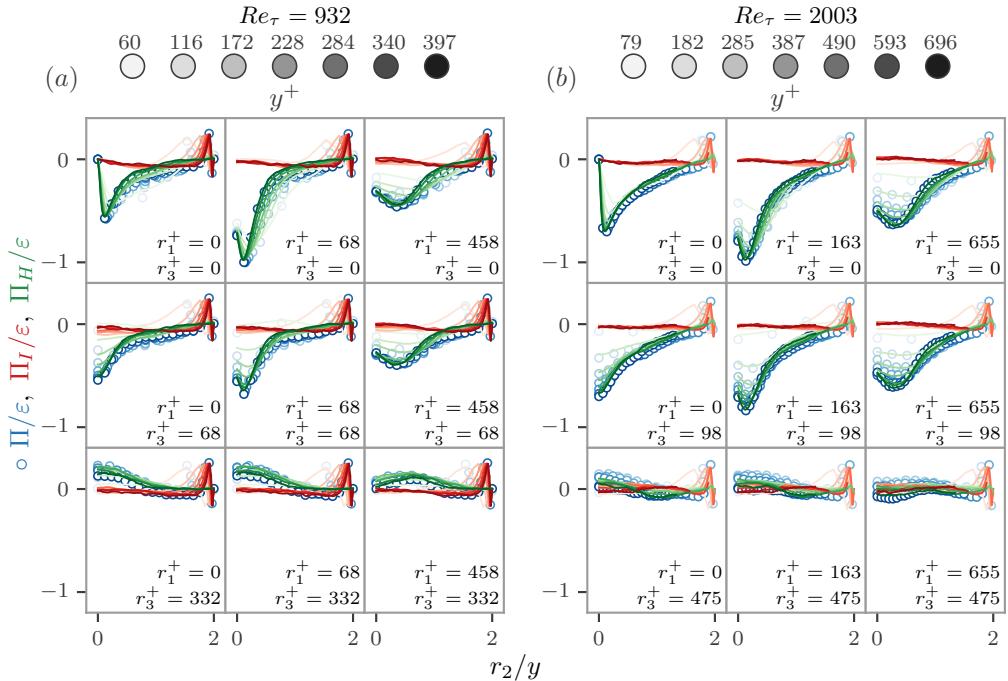


FIGURE 15.  $\Pi$  (blue markers),  $\Pi_I$  (red lines) and  $\Pi_H$  (green lines) normalised with the two point dissipation rate  $\varepsilon$  versus the wall-normal scale  $r_2$  divided with  $y$ . (a)  $Re_\tau = 932$ , from left to right we increase the streamwise scale  $r_1$  and from top to bottom the spanwise scale  $r_3$ . (b) Similarly for  $Re_\tau = 2003$ . Wall-normal distance is increased from light to dark colors.

610 normal distance  $y$  and various values of  $r_1$  and  $r_3$ , we find (figure 15) that  $\Pi_I(y, r_1, r_2, r_3)$   
 611 is close to 0 and negligible in most cases except for “attached eddies”, i.e. for values of  
 612  $r_2$  relatively close to  $2y$  (wall blocking implies  $r_2 \leq 2y$ ) where it is positive, thereby  
 613 potentially reflecting interscale transfer from small to large scales (similarly to Cimarelli  
 614 *et al.* 2016; Cho *et al.* 2018) except for  $r_2$  near-equal to  $2y$  where it is negative. The  
 615 non-vanishing inhomogeneity-related interscale transfer of “attached eddies” is averaged  
 616 out when we integrate  $\Pi_I$  to obtain  $\Pi_H^v$ .

617 Returning to  $\Pi_H^v$  and the fact that it has very similar dependencies on  $r$  and  $y$  as  $\Pi^v$ ,  
 618 we note in particular that  $\Pi_H^v$  has a minimum at the near same  $r \approx r_{\min}$  where  $\Pi^v$  has  
 619 a minimum, and even that the minimum value of  $\Pi_H^v$  closely obeys the same relation  
 620 6.21 that  $\Pi_{\min}^v$  obeys (see figure 16). As seen in section 6, the two-point separation scale  
 621  $r = r_{\min}$  demarcates between smaller values of  $r$  where  $\Pi^v$  is balanced by dissipation and  
 622 viscous diffusion and larger values of  $r$  where  $\Pi^v$  is balanced by dissipation and two-point  
 623 turbulence production. However, the theory of section 6, which is conclusive for  $\Pi^v$ , has  
 624 no say on  $\Pi_H^v$  and can therefore not explain our observation that  $\Pi_H^v$  behaves very much  
 625 like  $\Pi^v$ . We therefore adopt a different point of view from the one of section 6 and look at  
 626 PDFs of instantaneous (in time) and local (in  $(x, z)$  planes) interscale transfer rates  $\pi^v \equiv$   
 627  $\frac{3}{4\pi} \int \frac{\delta \mathbf{u} \cdot \hat{\mathbf{r}}}{r} |\delta \mathbf{u}|^2 d\Omega_r$ ,  $\pi_H^v \equiv -\frac{3}{2\pi} \int \frac{\delta \mathbf{u} \cdot \hat{\mathbf{r}}}{r} (\mathbf{u}^- \cdot \mathbf{u}^+) d\Omega_r$  and  $\pi_I^v \equiv \frac{3}{4\pi} \int \frac{\delta \mathbf{u} \cdot \hat{\mathbf{r}}}{r} (|\mathbf{u}^+|^2 + |\mathbf{u}^-|^2) d\Omega_r$ .  
 628 Clearly,  $\Pi^v = \langle \pi^v \rangle$ ,  $\Pi_H^v = \langle \pi_H^v \rangle$  and  $\Pi_I^v = \langle \pi_I^v \rangle$ .

629 In figure 17 we plot examples of PDFs of  $\pi^v$ ,  $\pi_H^v$  and  $\pi_I^v$  for a couple of wall distances  $y$   
 630 within the intermediate range  $\delta_\nu \ll y \ll \delta$  and for different values of separation scale  $r$  in  
 631 order to see how these PDFs evolve with varying  $r$ . As pointed out by Alves Portela *et al.*  
 632 (2020), at  $r = 0$  we have  $\Pi^v = \Pi_H^v = \Pi_I^v = 0$ . As  $r$  progressively increases, the PDFs of

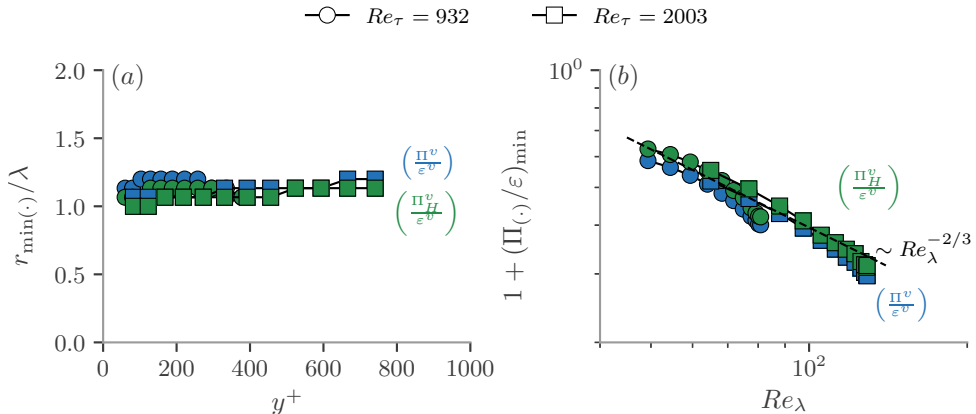


FIGURE 16. (a) Values of  $r/\lambda$  where minima of  $\Pi^v/\varepsilon^v$  and minima of  $\Pi_H^v/\varepsilon^v$  are observed as functions of wall distance  $y^+$ . (b) Values of  $1 + (\Pi^v/\varepsilon^v)_{\min}$  (in blue) and of  $1 + (\Pi_H^v/\varepsilon^v)_{\min}$  (in green), as functions of  $Re_\lambda$ . Dashed line shows a scaling of  $Re_\lambda^{-2/3}$ . Circle markers for  $Re_\tau = 932$ , square markers for  $Re_\tau = 2003$ .

633  $\pi^v$  and  $\pi_H^v$  move to the left towards increasingly negative values as shown in the inserts  
 634 of plots (a), (b), (e) and (f) in figure 17. This overall PDF drift is most pronounced at the  
 635 smaller values of  $r$  and causes  $\Pi^v$  and  $\Pi_H^v$  to progressively decrease below 0 as  $r$  increases.  
 636 However, the skewnesses of the PDFs of  $\pi^v$  and of  $\pi_H^v$  grow from negative values close  
 637 to  $-10$  at the smallest separations  $r$  to values between  $-1$  and even slightly positive as  
 638  $r$  grows (see plots (a), (b), (e) and (f) in figure 18). This evolution of the skewnesses of  
 639 these two PDFs counteracts their overall drift towards increasingly negative values and  
 640 acts to bring  $\Pi^v$  and  $\Pi_H^v$  back towards zero as  $r$  increases. The minima of  $\Pi^v$  and  $\Pi_H^v$   
 641 occur as a result of these two counteracting tendencies, the overall drift dominating at  
 642 scales  $r$  smaller than  $r_{\min}$  and causing  $\Pi^v$  and  $\Pi_H^v$  to decrease, the decreasingly skewed  
 643 PDF dominating at scales larger than  $r_{\min}$  and causing  $\Pi^v$  and  $\Pi_H^v$  to increase.

644 The PDF of the inhomogeneity-related interscale transfer rates  $\pi_I^v$  is radically different  
 645 as far as skewness is concerned (see figure 18). Whilst the PDFs of both  $\pi^v$  and  $\pi_H^v$  are  
 646 skewed towards forward cascade events at small  $r$  and evolve with increasing  $r$  towards not  
 647 being skewed or even being slightly skewed towards inverse cascade events, the PDF of  $\pi_I^v$   
 648 is highly skewed towards inverse cascade events at small  $r$  and evolves very quickly with  
 649 increasing  $r$  towards not being very skewed. It remains only slightly skewed (positively  
 650 or negatively) for all permissible  $r$  larger than about  $2\lambda$  (the word “permissible” refers to  
 651  $r \leq 2y$ ). The difference is not only that the PDF of  $\pi_I^v$  is oppositely skewed to the PDFs  
 652 of  $\pi^v$  and  $\pi_H^v$  at small  $r$ , the equally if not even more important difference is that, as  $r$   
 653 increases, the skewness of  $\pi_I^v$  evolves much faster towards small absolute values (which it  
 654 actually reaches at  $r \approx 2\lambda$ ) than the skewnesses of  $\pi_H^v$  and  $\pi^v$  which evolve much more  
 655 gradually towards values around and larger than  $-1$ .

656 On the other hand, the PDF of  $\pi_I^v$  is similar to the PDFs of  $\pi^v$  and  $\pi_H^v$  in that  
 657 they all have an overall drift to the left, i.e. towards forward cascading negative values,  
 658 as the separation scale  $r$  increases (see inserts of plots in figure 17). In the case of  
 659 the inhomogeneity-related interscale energy transfer rate, this overall PDF drift towards  
 660 forward cascade events is counteracted at small separations  $r$  by the significant PDF  
 661 skewness towards inverse cascade events leading to small values of  $\Pi_I^v$ . As  $r$  increases,  
 662 the drift slows down, and the skewness quickly drops to small absolute values keeping  
 663 values of  $\Pi_I^v$  small.



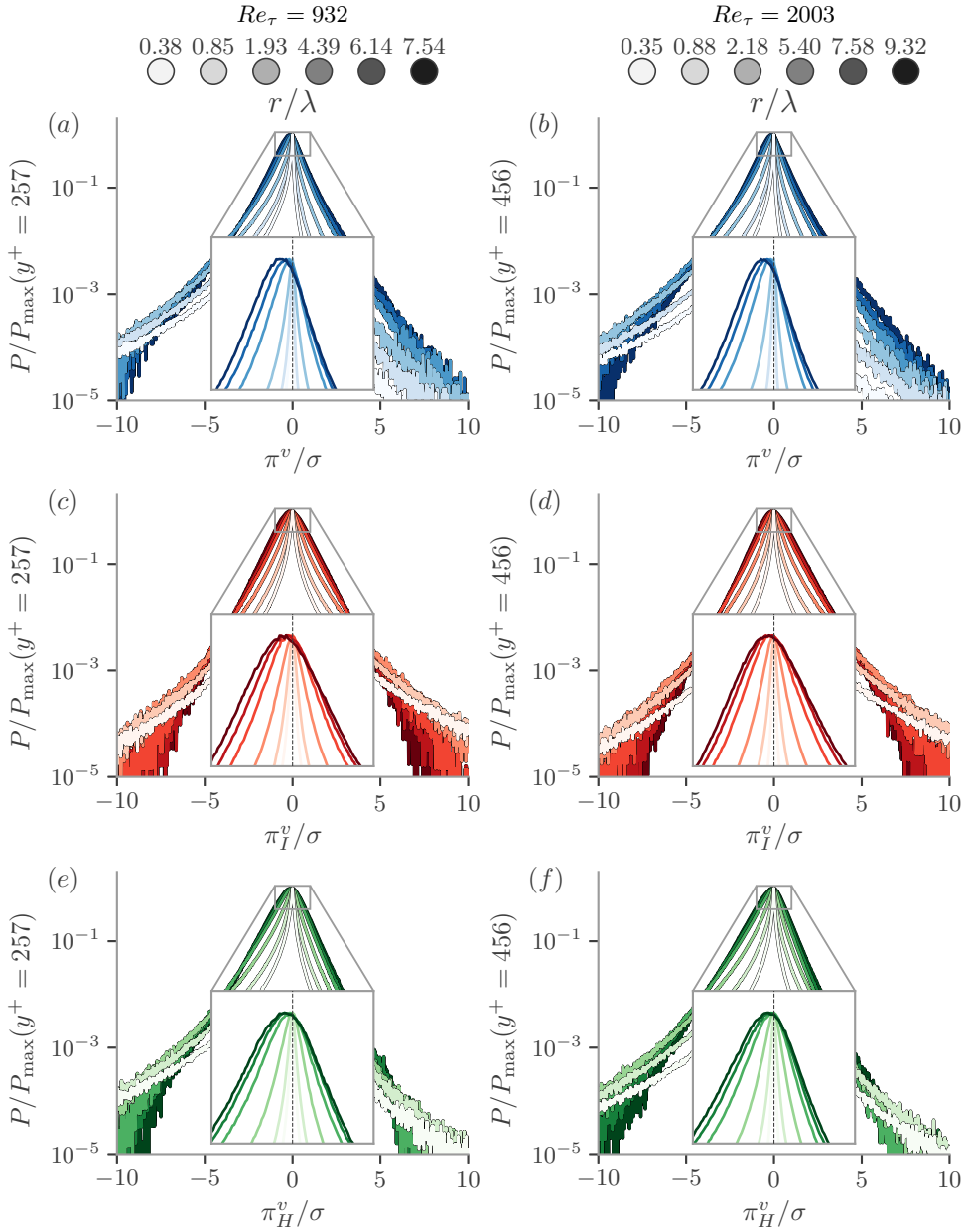


FIGURE 17. Probability density functions (PDFs) of (a,b):  $\pi^v$ , (c,d):  $\pi_I^v$  and (e,f):  $\pi_H^v$  normalised with their respective maximum probability. The values of the terms are normalised with their own standard deviation. From light to dark colors the scale  $r$  is increased. Left column:  $Re_\tau = 932$ , right column:  $Re_\tau = 2003$ . Inset is a zoom of the area close to the maximum probability in lin-lin axes.

664 In conclusion, the statistics of the inhomogeneity-related interscale transfer rate  $\pi_I^v$  are  
 665 very different from those of  $\pi_H^v$  and  $\pi^v$ . The PDFs of  $\pi_I^v$  are characterised by a skewness  
 666 towards inverse cascade events at the small scales in particular, whereas the PDFs of both  
 667  $\pi_H^v$  and  $\pi^v$  are characterised by a skewness towards forward cascade events at most scales.  
 668 These PDFs result in relatively small values of  $\Pi_I^v$  and in very similar dependencies on

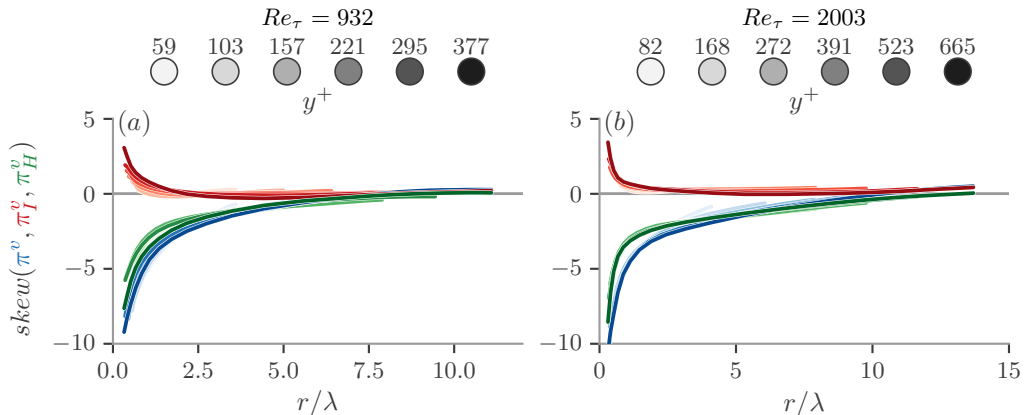


FIGURE 18. Skewness factor of  $\pi^v$  in blue colors,  $\pi_I^v$  in red colors and of  $\pi_H^v$  in green colors as a function of  $r/\lambda$ , for different wall-normal locations. From light to dark colors the wall-distance  $y$  is increased. (a) for  $Re_\tau = 932$  and (b) for  $Re_\tau = 2003$ .

669 separation  $r$  of  $\Pi_H^v$  and  $\Pi^v$ . As the separation scale  $r$  decreases from large values close  
 670 to  $2y$  towards the Taylor length  $\lambda$ , the PDFs of both  $\pi_H^v$  and  $\pi^v$  become increasingly  
 671 skewed towards forward cascading events and the average values  $\Pi_H^v$  and  $\Pi^v$  become  
 672 increasingly negative. However, as  $r$  crosses  $\lambda$  and tends towards even smaller separation  
 673 lengths below  $\lambda$ , these two PDFs drift towards inverse cascading events in their entirety,  
 674 thereby bringing the average values of  $\Pi_H^v$  and  $\Pi^v$  back towards zero.

675 These two counteracting effects of drift and skewness remain and are therefore confirmed  
 676 if we consider only the tails of the PDFs of  $\pi_H^v$  and  $\pi^v$ . In the top row of figure 19  
 677 (i.e. plots (a, b)), we plot the average values of  $\pi_H^v$  and  $\pi^v$  over the samples of relatively  
 678 intense values representing only 1% of all samples. The average of  $\pi_H^v$  over its relatively  
 679 intense values depends on  $y$  and  $r$  very much like  $\Pi_H^v$  but with an order of magnitude  
 680 higher values (compare with figure 14). On the other hand, the average of  $\pi_I^v$  over these  
 681 relatively intense values is disproportionately affected by the PDF's positive skewness and  
 682 is therefore positive or close to zero and higher than  $\Pi_I^v$  in figure 14 as the cancelling  
 683 effect of the drift is overcome. To concentrate on the drift and minimise the effect of  
 684 the skewness, in the second row of figure 19 (i.e. plots (c, d)) we report average values  
 685 of  $\pi_H^v$ ,  $\pi_I^v$  and  $\pi^v$  calculated on the basis of only the most probable part of the PDFs  
 686 representing 20% of all samples. These average values are an order of magnitude smaller  
 687 than  $\Pi_H^v$ ,  $\Pi_I^v$  and  $\Pi^v$  in figure 14. They are close to zero at the smallest separations  $r$  and  
 688 continuously decrease in negative values till they more or less stabilise at large enough  $r$ ,  
 689 reflecting the effect of overall drift of the PDFs towards forward interscale transfers and  
 690 the fact that this drift stabilises at large enough  $r$ . Without the skewness effect, which is  
 691 not as present around the peaks of the PDFs as in their extreme tails, these conditional  
 692 averages (plots (c, d) of figure 19) do not significantly return towards 0 with increasing  
 693  $r$  and therefore look very different from  $\Pi_H^v$ ,  $\Pi_I^v$  and  $\Pi^v$  in figure 14. The averages  $\Pi_H^v$ ,  
 694  $\Pi_I^v$  and  $\Pi^v$  in this latter figure emerge as a weighted sum of the conditional averages in  
 695 plots (a, b) with those in plots (c, d) of figure 19.

696 Note, finally, that the skewness dominated  $r$ -range of the PDFs of  $\pi_H^v$  and  $\pi^v$  coincides  
 697 with the  $r$ -range where  $\Pi^v$  is balanced by turbulent dissipation rate and two-point  
 698 turbulence production. The root cause of this coincidence may be anti-aligned velocity  
 699 fluctuation pairs because they enhance two-point turbulence production (section 5) while  
 700 also being the seat of a significant skewness towards compressive, i.e. forward cascading,

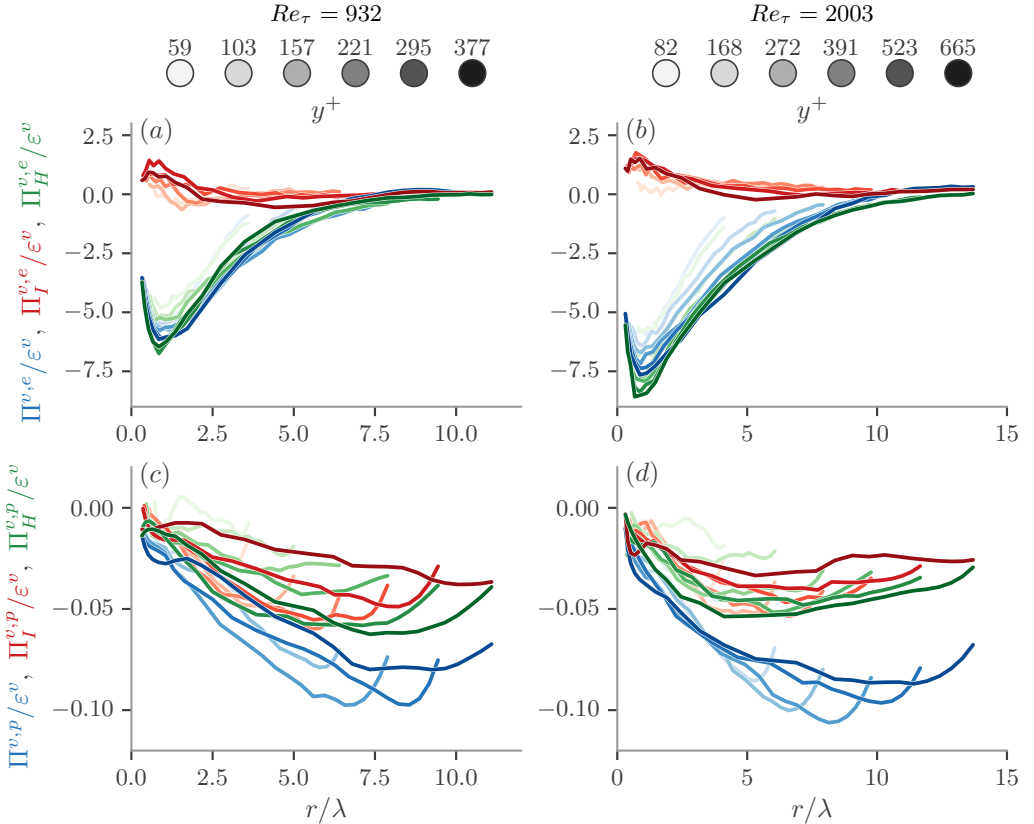


FIGURE 19. (a, b)  $\Pi^{v,e}$  (blue lines),  $\Pi_I^{v,e}$  (red lines) and  $\Pi_H^{v,e}$  (green lines): averages of most intense events accounting for 1% of all events. (c, d)  $\Pi^{v,p}$  (blue lines),  $\Pi_I^{v,p}$  (red lines) and  $\Pi_H^{v,p}$  (green lines): averages of most probable events accounting for 20% of all events. Left column (a, c) for  $Re_\tau = 932$ , right column (b, d) for  $Re_\tau = 2003$ . Wall-normal distance is increased from light to dark colors.

701 relative motions (sub-section 8.1). The drift of the PDFs of  $\pi_H^v$  and  $\pi^v$  towards inverse  
 702 cascades is in fact, a recentering of the PDFs so that their peak values move towards zero  
 703 and is mostly present in the  $r$ -range where  $\Pi^v$  is balanced by turbulent dissipation rate  
 704 and viscous diffusion (see section 6). At these small scales comparable to  $\lambda$  and below,  
 705 both aligned and anti-aligned fluctuation pairs contribute significantly to  $\Pi^v$  (see end  
 706 of sub-section 8.1) and this may be related to the recentering of the PDFs around zero  
 707 interscale transfer rate.

## 708 9. Conclusions

709 In this paper, we have considered fully developed turbulent channel flow (FD TCF) and  
 710 have made theoretical predictions concerning its scale-by-scale energy balance averaged  
 711 over spheres in  $\mathbf{r}$ -space in the double limit  $Re_\tau \rightarrow \infty$ ,  $y^+ \rightarrow \infty$  (i.e.  $Re_\lambda \sim \lambda/\delta_\nu \sim$   
 712  $(y^+)^{1/2} \rightarrow \infty$ ) with the constraint  $y \ll \delta$ . At leading order, both the inner and the  
 713 outer scale-by-scale energy balances involve interscale turbulence energy transfer and  
 714 turbulence dissipation, but the inner balance is completed with viscous diffusion, whereas  
 715 the outer balance is completed with two-point turbulence production.

716 Previous studies already analysed the Kármán–Howarth–Monin–Hill (KMH) equa-

717 tion for FD TCF. For example, Cimarelli *et al.* (2013, 2016) examined the energy flux path  
 718 in reduced spaces  $r_1$ ,  $r_3$  and  $y$  with  $r_2 = 0$  and  $r_2, r_3$  and  $y$  with  $r_1 = 0$  (or  $r_1 = \text{Const}$   
 719 in the case of Gatti *et al.* (2019)). The omission of one scale-space direction prevents this  
 720 approach from accessing the full interscale transfer picture. Our methodology is different  
 721 and complementary as it does not omit any scale-space direction but integrates over  
 722 spheres in full 3D scale space. Whilst we lose the ability to distinguish between directions  
 723 in scale space, we gain the capability to access decisive information on interscale energy  
 724 transfer and forward/inverse cascade which occur normal to the sphere’s surface in scale  
 725 space.

726 The intermediate layer ( $\delta_\nu \ll y \ll \delta$ ) of FD TCF is a non-homogeneous but statistically  
 727 stationary turbulent flow region where interscale turbulence energy transfer has proper-  
 728 ties similar to interscale turbulence energy transfer in freely decaying (i.e. non-stationary)  
 729 homogeneous turbulence far from initial conditions. This paper’s theory predicts that for  
 730 any wall-normal distance  $y$  in the intermediate layer, Kolmogorov equilibrium is achieved  
 731 asymptotically only around the Taylor length  $\lambda$  (i.e. for scales which are taken to remain  
 732 a constant multiple of  $\lambda$  in the asymptotic limit) which is not an inertial length given  
 733 that it depends on viscosity and turbulent kinetic energy at  $y$ . A similar conclusion was  
 734 reached in previous studies of freely decaying homogeneous turbulence far from initial  
 735 conditions (Lundgren 2002; Obligado & Vassilicos 2019; Meldi & Vassilicos 2021) where,  
 736 as shown here by equation 6.19 for the intermediate layer of FD TCF, there are systematic  
 737 departures from Kolmogorov equilibrium for scales moving away from  $\lambda$  both towards the  
 738 large eddy size (here  $y$ ) and towards the local (here in  $y$ ) Kolmogorov length  $\eta$ . DNS data  
 739 for FD TDF confirm these conclusions and also confirm the specific scaling predictions  
 740 6.20 and 6.21: namely, the interscale transfer rate has a forward cascade peak at  $r_{\min} \sim \lambda$   
 741 where it tends with increasing Reynolds number towards minus turbulence dissipation,  
 742 i.e. Kolmogorov-type equilibrium, as  $Re_\lambda^{-2/3}$ . Viscous diffusion is negligible on the large  
 743  $r$  side of this peak whereas turbulence production is negligible on the small  $r$  side of  
 744 the peak. A similar peak (where production’s role is played by the time derivative term  
 745 defined in section 2) and similar scalings hold in freely decaying homogeneous isotropic  
 746 turbulence far from initial conditions (Lundgren 2002; Obligado & Vassilicos 2019; Meldi  
 747 & Vassilicos 2021) but for slightly different though related quantities given that, here,  
 748 all the terms in the scale-by-scale turbulence energy budget are averaged over spheres of  
 749 radius  $r$  in  $\mathbf{r}$ -space.

750 The DNS data show that two-point turbulence production is positive for all  $r \leq 2y$  and  
 751 all  $y$  in the intermediate layer, and that it increases with two-point separation distance  $r$   
 752 and decreases with increasing  $y$ . The two-point turbulence production is positive mainly  
 753 because one-point turbulence production is positive even though two-point correlations  
 754 conditioned on more or less aligned fluctuating velocities act to reduce this positivity.  
 755 Interestingly, pairs of aligned fluctuating velocities may be expected mostly within sweeps  
 756 and ejections, which are regions with a major contribution to the positivity of one-  
 757 point turbulence production (Wallace 2016; Kline & Robinson 1990; Pope 2000). The  
 758 positivity of two-point turbulence production is in fact enhanced by two-point correlations  
 759 conditioned on more or less anti-aligned fluctuating velocities, particularly at larger  
 760 separations  $r$ .

761 The two-point production rate is a functional (see 4.8) of the second order anisotropic  
 762 structure function  $S_{12}$  defined by 4.6. This structure function is identically zero in  
 763 homogeneous isotropic turbulence, but in the intermediate layer of FD TCF the present  
 764 theory predicts a leading order  $(\varepsilon^v r)^{2/3} \sim u_\tau^2 (r/y)^{2/3}$  behaviour for  $S_{12}$  in the range  
 765  $\eta \ll r \ll y$ . The DNS data provide some, though not entirely conclusive, confirmation

766 for this high Reynolds number scaling but the values of  $Re_\lambda$  are probably not high enough  
 767 (between 50 and 120) in the DNS data used here for which  $Re_\tau$  is about 2000 in one case  
 768 and about 1000 in the other.

769 The present asymptotically high Reynolds number theory also leads to a leading order  
 770 scaling for the second order structure function  $S_2$  which is similar to the centreline  
 771 region of some turbulent wakes in terms of the  $r^{2/3}$  part of the scaling but different  
 772 in terms of the prefactor which is not proportional to the  $2/3$  power of a turbulence  
 773 dissipation rate in the centreline region of those turbulent wakes (see Chen & Vassilicos  
 774 2022). Different types of non-homogeneity may lead to some important differences in  
 775 second order structure function scalings, an issue which merits future attention. The non-  
 776 homogeneity in the intermediate layer of FD TCF is characterised by significant two-point  
 777 turbulence production and negligible two-point turbulent transport and pressure-velocity  
 778 terms, whereas the non-homogeneity on the centreline of turbulent wakes is inverse, i.e.  
 779 turbulent production is negligible but turbulent transport and pressure-velocity terms  
 780 are not. Future attempts at a physically meaningful classification of non-homogeneous  
 781 turbulent flows may need to start from this paragraph's observations.

782 The opposing roles played by more or less aligned and more or less anti-aligned pairs  
 783 of fluctuating velocities in shaping two-point turbulence production have motivated the  
 784 second part of our DNS study concerning their roles in shaping interscale turbulence  
 785 energy transfer in the intermediate layer of FD TCF. The interscale turbulence energy is  
 786 determined by stretching relative motions responsible for inverse transfer from small  
 787 to large scales and by compressing relative motions responsible for forward transfer  
 788 from large to small scales. It turns out that more or less aligned fluctuation pairs are  
 789 stretching relative motions on average whereas more or less anti-aligned fluctuation pairs  
 790 are on average compressive relative motions. The relative motions of more or less aligned  
 791 fluctuation pairs are stretching on average as a result of  $\delta\mathbf{u}$  having a tendency to be  
 792 directed in the same direction as the separation vector  $\mathbf{r}$  for pairs of aligned fluctuating  
 793 velocities, a tendency which weakens with increasing  $r$  irrespective of wall distance  $y$ . The  
 794 relative motions of more or less anti-aligned fluctuation pairs are compressive on average  
 795 because the fluctuations of  $\delta\mathbf{u} \cdot \hat{\mathbf{r}}$  are skewed towards negative values for such fluctuation  
 796 pairs. This skewness diminishes with increasing  $r$  irrespective of  $y$ . Incidentally, more  
 797 or less aligned fluctuation pairs are much more likely than more or less anti-aligned  
 798 fluctuation pairs.

799 Relative motions of more or less aligned fluctuation pairs are maximally stretching on  
 800 average, and relative motions of more or less anti-aligned fluctuation pairs are maximally  
 801 compressing on average at a separation length  $r = r_m$  which, for all  $y$ , is very close  
 802 to  $r_{\min}$ , the separation length where  $\Pi^v/\varepsilon^v$  has its minimum. Combining the first and  
 803 second parts of the present study, it appears that, in the layer  $\delta_\nu \ll y \ll \delta$  of FD TCF,  
 804 an approach to Kolmogorov-like equilibrium with increasing local Reynolds number may  
 805 be achieved at those length scales  $r$  where aligned fluctuating velocities are stretching  
 806 with their difference  $\delta\mathbf{u}$  maximally or near-maximally aligned with the separation vector  
 807  $\mathbf{r}$  and where anti-aligned fluctuations are maximally or near-maximally skewed towards  
 808 large negative values of  $\delta\mathbf{u} \cdot \hat{\mathbf{r}}$ .

809 Even though more or less aligned fluctuation pairs are on average stretching and are  
 810 more frequent than more or less anti-aligned fluctuation pairs, they do not dominate  
 811 interscale turbulence energy transfer, which is nevertheless forward on average, i.e. from  
 812 large to small scales. This is an effect of small-scale anisotropies. At scales of the order  
 813 of the Taylor length and larger the interscale turbulence energy transfer is, in fact,  
 814 dominated by more or less anti-aligned fluctuations. However, at scales smaller than  
 815 the Taylor length, the actual value of the interscale turbulence energy transfer rate

816 results from interscale turbulence energy transfers by both aligned (local inverse cascades)  
 817 and anti-aligned (local forward cascades) fluctuations, both of which are significant and  
 818 cannot be ignored.

819 Finally, correlations between stretching/compression relative motions and alignment/anti-  
 820 alignment of fluctuation pairs determine the spherically averaged (in  $\mathbf{r}$ -space)  
 821 homogeneous part of the interscale turbulence energy transfer rate introduced by  
 822 Alves Portela *et al.* (2020). The DNS data of FD TCF used here, show that this  
 823 homogeneous part accounts almost completely for the total spherically averaged  
 824 interscale turbulence energy transfer rate in the intermediate layer for all separation  
 825 scales  $r \leq 2y$ , including the scaling with the Taylor length of the separation  $r = r_{\min}$   
 826 where it peaks and the scaling with  $Re_\lambda$  of its peak value, i.e. scalings 6.20 and 6.21. The  
 827 spherically averaged inhomogeneous part of the interscale turbulence energy transfer  
 828 is negligible even though the turbulence is significantly non-homogeneous in FD TCF  
 829 in contrast with the centerline of a turbulent wake which is also non-homogeneous,  
 830 but differently, and where Alves Portela *et al.* (2020) found a similarly averaged  
 831 inhomogeneous interscale turbulence energy transfer to be significant and in fact quite  
 832 important in the scale-by-scale physics. However, when the spherical average is lifted,  
 833 the average inhomogeneous interscale transfer rate remains close to zero except for  
 834 separation components  $r_2$  characterising attached eddies.



835 By lifting the average over  $x, z, t$ , we obtain PDFs of spherically averaged interscale  
 836 turbulence energy transfer rates and of their homogeneous and inhomogeneous parts.  
 837 The PDFs of the spherically averaged interscale turbulence energy transfer rates and  
 838 of their homogeneous part are very similar and vary with  $r$  in a very similar way.  
 839 Their dependence on  $r$  is governed by counteracting effects of overall PDF drift towards  
 840 forward cascade values and of diminishing skewness towards forward cascade events with  
 841 increasing  $r$ . The approach towards Kolmogorov equilibrium occurs at those scales  $r$  near  
 842 the Taylor length where these two counteracting effects balance. The PDFs of spherically  
 843 averaged inhomogeneous interscale turbulence energy transfer rates are significantly  
 844 different as they are characterised by a skewness towards inverse rather than forward  
 845 cascade events at small scales.

846 As a final comment, one area that may reveal more information on energy transfer in  
 847 wall-turbulence should be the application of the present paper's framework to individual  
 848 structural elements of the flow such as intense Reynolds shear stress structures (Lozano-  
 849 Durán & Jiménez 2014), vortex clusters (del Álamo *et al.* 2006) and uniform momentum  
 850 zones and vortical fissures (Bautista *et al.* 2019).

851 **Acknowledgements.** This work was supported by the European Community, the French  
 852 Ministry for Higher Education and Research and the Hauts de France Regional Council in  
 853 connection with CNRS Research Foundation on Ground Transport and Mobility as part of the  
 854 ELSAT2020 project. The work was granted access to the HPC resources of IDRIS under the  
 855 allocation 2021-021741 made by GENCI (Grand Equipement National de Calcul Intensif). We  
 856 are also grateful A. Lozano-Durán and J. Jiménez for making their datasets available and to  
 857 Marcello Meldi for suggesting the plot (b) in figure 6 as a check.

858 **Funding.** This work was directly supported by JCV's Chair of Excellence CoPreFlo funded by  
 859 I-SITE-ULNE (grant number R-TALENT-19-001-VASSILICOS), MEL (grant number CON-  
 860 VENTION\_219\_ESR\_06) and Region Hauts de France (grant number 20003862); and by ERC  
 861 Advanced Grant NoStaHo funded by the European Union. Views and opinions expressed are  
 862 however those of the authors only and do not necessarily reflect those of the European Union or  
 863 of the European Research Council Executive Agency (ERCEA). Neither the European Union  
 864 nor the granting authority can be held responsible for them.

865 **Declaration of interests.** The authors report no conflict of interest.

866 **Author ORCIDs.**867  A. Apostolidis <https://orcid.org/0000-0002-9078-1490>;868  J.P. Laval <https://orcid.org/0000-0003-2267-8376>;869  J.C. Vassilicos <https://orcid.org/0000-0003-1828-6628>.870 **Appendix A.**

871 We use two methods for the numerical computation of the normalised 3D integrals of  
 872 equation 2.2. The volume integrals that involve divergence in  $\mathbf{r}$  space are simplified using  
 873 the Gauss divergence theorem and therefore transformed into surface integrals of the flux  
 874 across the sphere's surface. We insert a triangulated sphere of 5120 triangles and radius  
 875  $r$  at each  $x, y, z$  point of the DNS grid, corresponding to the centre of the sphere, and  
 876 interpolate the velocity and its derivatives, using a trilinear interpolation, at the centres  
 877 of the triangles. Finally, we compute the two-point quantities of interest between the  
 878 antipodal triangles on our sphere, multiply them with the corresponding surface area of  
 879 the triangle, sum all the triangles and divide the result with the volume of the discretised  
 880 sphere.

881 For the quantities that we cannot apply the Gauss divergence theorem, we make a local  
 882 cartesian grid of  $n_{x_l} = 41, n_{y_l} = 81, n_{z_l} = 41$  points centred at each  $x, y, z$  point in space,  
 883 corresponding to the centre of the sphere, and extending from  $-r$  to  $r$  in all directions.  
 884 We then interpolate (with trilinear interpolation) the velocity and its derivatives at every  
 885 point, which satisfies  $\sqrt{x_l^2 + y_l^2 + z_l^2} \leq r$  ( $x_l, y_l, z_l$  are the local coordinates), compute  
 886 the two-point quantities and multiply them with the local volume unit  $dV_l = dx_l dy_l dz_l$ ,  
 887 sum and divide with the volume of the discretised sphere.

## REFERENCES

- 888 ALVES PORTELA, F., PAPADAKIS, G. & VASSILICOS, J. C. 2020 The role of coherent structures  
 889 and inhomogeneity in near-field interscale turbulent energy transfers. *Journal of Fluid*  
 890 *Mechanics* **896**, A16.
- 891 APOSTOLIDIS, A., LAVAL, J.-P. & VASSILICOS, J. C. 2022 Scalings of turbulence dissipation in  
 892 space and time for turbulent channel flow. *Journal of Fluid Mechanics* **946**, A41.
- 893 BATCHELOR, GEORGE KEITH 1953 *The theory of homogeneous turbulence*. Cambridge university  
 894 press.
- 895 BAUTISTA, JUAN CARLOS CUEVAS, EBADI, ALIREZA, WHITE, CHRISTOPHER M., CHINI,  
 896 GREGORY P. & KLEWICKI, JOSEPH C. 2019 A uniform momentum zone–vortical fissure  
 897 model of the turbulent boundary layer. *Journal of Fluid Mechanics* **858**, 609–633.
- 898 CHEN, J. G. & VASSILICOS, J. C. 2022 Scalings of scale-by-scale turbulence energy in non-  
 899 homogeneous turbulence. *Journal of Fluid Mechanics* **938**, A7.
- 900 CHO, MINJEONG, HWANG, YONGYUN & CHOI, HAECHON 2018 Scale interactions and spectral  
 901 energy transfer in turbulent channel flow. *Journal of Fluid Mechanics* **854**, 474–504.
- 902 CIMARELLI, A. & DE ANGELIS, E. 2012 Anisotropic dynamics and sub-grid energy transfer in  
 903 wall-turbulence. *Physics of Fluids* **24** (1), 015102.
- 904 CIMARELLI, A., DE ANGELIS, E. & CASCIOLA, C. M. 2013 Paths of energy in turbulent channel  
 905 flows. *Journal of Fluid Mechanics* **715**, 436–451.
- 906 CIMARELLI, ANDREA, DE ANGELIS, ELISABETTA, JIMENEZ, JAVIER & CASCIOLA,  
 907 CARLO MASSIMO 2016 Cascades and wall-normal fluxes in turbulent channel flows. *Journal*  
 908 *of Fluid Mechanics* **796**, 417–436.
- 909 COLE, JULIAN D. 1968 *Perturbation Methods in Applied Mathematics*. Blaisdell Publishing  
 910 Company, Waltham.
- 911 DALLAS, V., VASSILICOS, J. C. & HEWITT, G. F. 2009 Stagnation point von Kármán coefficient.  
 912 *Phys. Rev. E* **80** (4), 046306.
- 913 DEL ÁLAMO, JUAN C., JIMÉNEZ, JAVIER, ZANDONADE, PAULO & MOSER, ROBERT D. 2006

- 914 Self-similar vortex clusters in the turbulent logarithmic region. *Journal of Fluid Mechanics*  
915 **561**, 329.
- 916 FRISCH, U. 1995 *Turbulence: The Legacy of A.N. Kolmogorov*. Cambridge University Press.
- 917 GATTI, DAVIDE, REMIGI, ALBERTO, CHIARINI, ALESSANDRO, CIMARELLI, ANDREA & QUADRIO,  
918 MAURIZIO 2019 An efficient numerical method for the generalised Kolmogorov equation.  
919 *Journal of Turbulence* **20** (8), 457–480.
- 920 GOTO, SUSUMU & VASSILICOS, J. C. 2016 Unsteady turbulence cascades. *Physical Review E*  
921 **94** (5), 053108.
- 922 HILL, REGINALD J 2001 Equations relating structure functions of all orders. *Journal of Fluid*  
923 *Mechanics* **434**, 379–388.
- 924 HILL, REGINALD J. 2002 Exact second-order structure-function relationships. *Journal of Fluid*  
925 *Mechanics* **468**, 317–326.
- 926 HINCH, E. J. 1991 *Perturbation Methods*. Cambridge University Press.
- 927 KLINE, SJ & ROBINSON, SK 1990 Quasi-coherent structures in the turbulent boundary layer.  
928 i-status report on a community-wide summary of the data. *Near-wall turbulence* pp. 200–  
929 217.
- 930 LEE, MYOUNGKYU & MOSER, ROBERT D. 2019 Spectral analysis of the budget equation in  
931 turbulent channel flows at high Re. *Journal of Fluid Mechanics* **860**, 886–938, arXiv:  
932 1806.01254.
- 933 LESIEUR, MARCEL 1997 *Turbulence in Fluids, Fluid Mechanics and Its Applications*, vol. 40.  
934 Dordrecht: Springer Netherlands.
- 935 LOZANO-DURÁN, A. & JIMÉNEZ, J. 2014 Time-resolved evolution of coherent structures in  
936 turbulent channels: Characterization of eddies and cascades. *Journal of Fluid Mechanics*  
937 **759**.
- 938 LUNDGREN, THOMAS S 2002 Kolmogorov two-thirds law by matched asymptotic expansion.  
939 *Phys. Fluids* **14** (2), 6.
- 940 MARATI, N., CASCIOLA, C. M. & PIVA, R. 2004 Energy cascade and spatial fluxes in wall  
941 turbulence. *Journal of Fluid Mechanics* **521**, 191–215.
- 942 MELDI, MARCELLO & VASSILICOS, J. C. 2021 Analysis of lundgren’s matched asymptotic  
943 expansion approach to the k<sup>2</sup> armán-howarth equation using the eddy damped quasinormal  
944 markovian turbulence closure. *Physical Review Fluids* **6** (6), 064602.
- 945 OBLIGADO, M & VASSILICOS, J. C. 2019 The non-equilibrium part of the inertial range in  
946 decaying homogeneous turbulence. *EPL (Europhysics Letters)* **127** (6), 64004.
- 947 POPE, S. B. 2000 *Turbulent Flows*. Cambridge; New York: Cambridge University Press.
- 948 SAGAUT, PIERRE & CAMBON, CLAUDE 2018 *Homogeneous Turbulence Dynamics*. Springer  
949 International Publishing.
- 950 SREENIVASAN, KATEPALLI R 1984 On the scaling of the turbulence energy dissipation rate. *The*  
951 *Physics of fluids* **27** (5), 1048–1051.
- 952 STEIROS, KONSTANTINOS 2022 Balanced nonstationary turbulence. *Physical Review E* **105** (3),  
953 035109.
- 954 TAYLOR, GEOFFREY INGRAM 1935 Statistical theory of turbulence. *Proceedings of the Royal*  
955 *Society of London. Series A-Mathematical and Physical Sciences* **151** (873), 421–444.
- 956 TOWNSEND, ALBERT A. 1976 *The Structure of Turbulent Shear Flow*, 2nd edn. Cambridge:  
957 Cambridge Univ. Press.
- 958 VAN DYKE, M. D. 1964 *Perturbation Methods in Fluid Mechanics*. Academic Press, New York  
959 and London.
- 960 VASSILICOS, J. C. 2015 Dissipation in turbulent flows. *Annu. Rev. Fluid Mech* **47** (1), 95–114.
- 961 VASSILICOS, J. C., LAVAL, J.-P., FOUCAUT, J.-M. & STANISLAS, M. 2015 The streamwise  
962 turbulence intensity in the intermediate layer of turbulent pipe flow. *Journal of Fluid*  
963 *Mechanics* **774**, 324–341.
- 964 WALLACE, JAMES M. 2016 Quadrant Analysis in Turbulence Research: History and Evolution.  
965 *Annual Review of Fluid Mechanics* **48** (1), 131–158.
- 966 YUVARAJ, R. 2022 Analysis of energy cascade in wall-bounded turbulent flows. PhD thesis,  
967 Centrale Lille Institut.
- 968 ZHOU, Y. & VASSILICOS, J. C. 2020 Energy cascade at the turbulent/nonturbulent interface.  
969 *Phys. Rev. Fluids* **5**, 064604.
- 970 ZIMMERMAN, SPENCER J., ANTONIA, R. A., DJENIDI, L., PHILIP, J. & KLEWICKI, J. C.



971 2022 Approach to the  $4/3$  law for turbulent pipe and channel flows examined through a  
972 reformulated scale-by-scale energy budget. *Journal of Fluid Mechanics* **931**.